

1 Inter-model variability of future changes in the Baiu rainband estimated
2 by the Pseudo-Global Warming Downscaling method

3

4 Hiroaki Kawase

5 National Institute for Environmental Studies, Tsukuba, Japan

6 Takao Yoshikane, Masayuki Hara, Fujio Kimura,¹ and Tetsuzo Yasunari²

7 Research Institute for Global Change, Yokohama, Japan

8 Borjiginte Ailikun

9 Institute of Atmospheric Physics, Chinese Academy of Science, Beijing, P.R. China

10 Hiroaki Ueda and Tomoshige Inoue

11 Graduate School of Life and Environmental Sciences, University of Tsukuba, Tsukuba, Japan

12 _____

13 1 Additional affiliation: Graduate School of Life and Environmental Sciences, University
14 of Tsukuba, Tsukuba, Japan

15 2 Additional affiliation: Hydrospheric Atmospheric Research Center, Nagoya University,
16 Nagoya, Japan

17

1 Abstract

2 Changes in the Baiu rainband due to global warming are assessed by the
3 Pseudo-Global Warming Downscaling method (PGW-DS). The PGW-DS is almost the
4 same as the conventional dynamical downscaling method using a regional climate model
5 (RCM), but the boundary conditions of the RCM are obtained by adding the difference
6 between the future and present climates simulated by coupled general circulation models
7 (CGCMs) into the six-hourly reanalysis data in a control period.

8

9 We conducted the multiple PGW-DS runs using selected CMIP3 multi-model dataset
10 giving better performance of around East Asia in June and the PGW-DS run using the
11 multi-selected CGCM ensemble mean (PGW-MME run). The PGW-MME and PGW-DS
12 runs show an increase in precipitation over the Baiu rainband and the southward shift of
13 the Baiu rainband. The PGW-MME run has good similarity to the average of all PGW-DS
14 runs. This fact indicates that an average of the multi-PGW-DS runs can be replaced by a
15 single PGW-DS run using the multi-selected CGCM ensemble mean, reducing the
16 significant computational expense. In comparison with the GCM projections, the PGW-DS

1 runs reduce the inter-model variability in the Baiu rainband caused by the CGCMs

2 themselves.

3

1. Introduction

The Baiu/Meiyu/Changma front, as it called in Japan/China/Korea, is strongly related to the Asian Summer Monsoon (ASM) and brings a large amount of rainfall over East Asia in summer (hereafter, referred to as the Baiu rainband) [Kurashima and Hiranuma, 1971].

The climatic variation in the Baiu rainband causes not only frequent serious flooding but also occasional droughts in East Asia. The Intergovernmental Panel on Climate Change (IPCC) [2001, 2007] reported that the increase in greenhouse gases could change the ASM intensity and duration, resulting in changes in the Baiu rainband in the future.

The Ocean-Atmosphere Coupled General Circulation Models (CGCMs) have been used to investigate climate changes due to an increase of greenhouse gases. The analysis method using the multiple CGCM ensemble mean (hereafter, the MME mean) is effective for the improvement of projections due to the reduction of biases and uncertainties of individual CGCMs [e.g., Giorgi and Mearns, 2002]. Climate changes were investigated using the MME mean obtained from the WCRP Coupled Model Intercomparison Project phase 3 (CMIP3) multi-model dataset [Meehl et al., 2007] during the ASM season [Min et

1 *al.*, 2004; *Ueda et al.*, 2006; *Kitoh and Uchiyama*, 2006]. The activity of the ASM would
2 be enhanced in association with the strengthening of anti-cyclonic circulations to its south
3 and north [*Kimoto*, 2005], resulting in the change in the Baiu rainband.

4

5 The simulation of the Baiu rainband is extremely difficult for GCMs due to the lack
6 of resolution as well as to shortcomings in the physical process parameterizations [*Kang et*
7 *al.*, 2002; *Ninomiya et al.*, 2002]. *Kawatani and Takahashi* [2003] demonstrated that the
8 structures of the Baiu front, from large scale to meso-alpha scale, were well simulated in a
9 high-resolution AGCM with a grid size of about 110 km. A comparison of high- and
10 medium-resolution CGCMs showed that the higher-resolution version better reproduced
11 not only the mean precipitation but also the frequency of precipitation over Japan in the
12 warm season in the present climate [*Kimoto, et al.* 2005]. The time-slice experiment was
13 conducted using a very high-resolution AGCM with 20-km grid size developed by the
14 Japan Meteorological Agency (JMA) and the Meteorological Research Institute (MRI)
15 (hereafter, MRI 20-km AGCM) [*Mizuta et al.*, 2006]. In comparison with lower-resolution
16 model experiments, the MRI 20-km AGCM showed superiority in simulating orographic

1 rainfall regarding not only its location but also its amount [*Kusunoki et al.*, 2006].

2

3 Downscaling methods are the techniques to complement the GCM simulations with
4 the detailed temporal and spatial structures. Two major downscalings have been proposed:
5 one is a statistical downscaling, and the other is a dynamical downscaling (DDS). A
6 conventional DDS consists of a numerical simulation using a regional climate model
7 (RCM). The RCM applies the GCM outputs to the initial and boundary conditions. *Wang et*
8 *al.* [2004] stated the history of the development of DDSs. Original RCMs were conducted
9 using the hydrostatic primitive equations. With the development of computational
10 performances, some RCMs have been converted into models based on non-hydrostatic
11 equations. *Kato et al.* [2001] were concerned that the regional climate changes were
12 mainly influenced by the reproducibility of the present climate simulated by the GCM and
13 indicated that the GCM should be of a good quality when the regional climate was
14 estimated in detail by the DDSs.

15

16 Using the RCM with a 20-km grid size, *Kurihara et al.* [2005] indicated that the

1 precipitation would increase during the warm season in Western Japan because the
2 intensification of the anti-cyclonic circulation over the east Pacific Ocean resulted in strong
3 moisture flux convergence over Western Japan in the late 21st Century under the Special
4 Report on Emissions Scenario A2 (SRES-A2) scenario by the *IPCC* [2000]. More detailed
5 changes in the Baiu rainband due to global warming were investigated using a
6 non-hydrostatic cloud-resolving regional climate model (NHM). The initial and lateral
7 boundary conditions were obtained from the outputs of the MRI 20-km AGCM under the
8 SRES-A1B scenario [*Yasunaga et al.*, 2006]. The Baiu front was likely to stay over the
9 southern Japan Islands and did not move northward in summer in the global warming
10 climate [*Yoshizaki et al.*, 2005].

11

12 A new concept of the DDS called Pseudo-Global Warming Downscaling method
13 (hereafter PGW-DS) was proposed by *Kimura and Kitoh* [2007] and adopted for some
14 regions [*Sato et al.*, 2007; *Hara et al.*, 2008]. The PGW-DS is almost the same as the
15 conventional DDS, but the boundary condition of the RCM is a composite of six-hourly
16 reanalysis data and the differences in monthly mean variables between the present and the

1 future climates simulated by CGCMs. *Knutson et al.* [2008] applied a similar method to the
2 Atlantic hurricanes and found that Atlantic hurricane and tropical storm frequencies would
3 be reduced and near-storm rainfall rates would increase substantially under the pseudo
4 atmospheric state and sea surface temperature (SST) in the 21st century. *Frei et al.* [1998]
5 conducted a similar DDS to the PGW-DS to investigate heavy precipitation processes in a
6 warmer climate in Europe, but they considered only the effects of uniform temperature rise
7 and relevant changes in other atmospheric variables.

8

9 *Kawase et al.* [2008] applied the PGW-DS to the past climatic change in the
10 distribution of the Baiu rainband over China between the 1960s and 1990s during early
11 summer. They discussed two advantages of the PGW-DS. One is the reduction of the
12 model bias contained in the GCMs, and the other is the circumventing of the uncertainty
13 caused by the interannual variability even in the case of a shorter integration period, such
14 as 10 years. It is, however, difficult to evaluate the changes in the interannual variability
15 and the frequencies of disturbances because the PGW-DS assumes unchanged variability
16 even in the future climate. The uncertainty caused by the change in the variability still

1 remains.

2

3 The PGW-DS easily enables multiple DDSs under multiple CGCMs because it
4 requires only monthly mean atmospheric variables and sea surface temperature, both of
5 which can be much more easily obtained than six-hourly data. This reduces the need to
6 archive and access CGCM data. The purpose of this study is to assess future changes in the
7 Baiu rainband using the PGW-DS. We focus on June when the stable Baiu rainband
8 appears around Southern China and Japan.

9

10

1 2. Reproducibility of Present Climate and Projections by CGCMs

2 The CGCMs have various biases in the simulation of present regional climate, e.g.,
3 in East Asia, which would result in a large uncertainty in the projections of regional
4 climate change due to global warming. The PGW-DS relies on the differences between
5 present and future climates simulated by CGCMs. The selection of CGCMs with high
6 performance of the present climate is essential to conduct the PGW-DS, although this
7 method reduces the effects of the CGCM bias in the present climate more than the
8 conventional DDS.

9

10 A new type of diagram (hereafter, the Taylor diagram) and skill scores were
11 proposed by *Taylor* [2001] to evaluate CGCM performances. The Taylor diagram relates
12 the centered Root Mean Square Error (RMSE), the pattern correlation, and the standard
13 deviation. The performances of CGCMs in Asia have also been evaluated using the Taylor
14 diagram in previous studies [*Min et al.*, 2004; *Kusunoki et al.*, 2006; Inoue and Ueda,
15 2009]. The Taylor diagram and skill score make it possible to evaluate the location and
16 strength of the Baiu rainband simulated by the CGCMs.

1

2 Table 1 shows the 15 CGCMs with the necessary atmospheric and surface variables

3 to conduct the PGW-DS, which are available at the CMIP3 multi-model dataset. The

4 present climate is obtained from the 20th Century Climate in Coupled Models (20C3M).

5 References of precipitation and 850 hPa wind are derived from CPC Merged Analysis of

6 Precipitation (CMAP) [*Xie and Arkin, 1997*] and ECMWF 40-year Re-Analysis (ERA40)

7 Data [*Uppala et al., 2005*], respectively. We define the analyzed period as 1980-1999 for

8 comparison with CMAP precipitation data. The analyzed area is Region A, shown in Fig. 1.

9 All models are interpolated into the same 2.5°×2.5° grids as the reference data.

10

11 The skill score (S) is defined as

12
$$S = \frac{4(1 + R)^4}{(SDR + 1/SDR)^2(1 + R_0)^4},$$

13 where R, R₀, and SDR are, respectively, the correlation coefficient, the maximum

14 correlation attainable, which is equal to the mean of the intra-ensemble correlation values,

15 and the model standard deviation divided by the standard deviation of the corresponding

16 observed field [*Taylor, 2001*]. Here, we assume R₀ = 1.0. High skill scores mean that the

1 spatial patterns of the realistic climate are well simulated by the CGCMs. More detailed
2 information is provided in *Taylor* [2001]. We select seven CGCMs, i.e., CCCMA, CNRM,
3 GFDL21, INGV, MIROCM, MIROCH, and MRI, which have higher skill scores for
4 precipitation than the average of all models. Both the MIROCM and the MIROCH are
5 selected to focus on the difference in resolutions, but we only use one later version of the
6 GFDL model, GFDL21.

7

8 The seven selected CGCMs show higher correlation coefficients for precipitation in
9 the range between 0.6 and 0.8 than the other CGCMs (Fig. 2a). On the other hand, the
10 standard deviations of the selected CGCMs are smaller than those of the reference data,
11 except for the MIROCH and the MRI. The skill score of the ensemble mean of the seven
12 CGCMs (hereafter, MME-CGCM) is the highest in Fig. 2a, as reported in previous studies
13 [e.g., *Min et al.*, 2004].

14

15 The selected CGCMs, except for CCCMA, show quite high correlation coefficients
16 of about 0.9 for the 850 hPa zonal wind component (Fig. 2b). Their standard deviations are,

1 however, scattered. The standard deviations of the MRI and the GFDL are similar to those
2 of the reference data. The selected CGCMs are plotted more scattered on the Taylor
3 diagram for the meridional wind component (Fig. 2c) than for the zonal wind component.
4 The MME-CGCM shows the highest skill score for the zonal and meridional winds as well
5 as the precipitation.

6
7 Figure 3 shows 30-year mean precipitation in June from 2060 to 2089 simulated by
8 the MME-CGCM and the seven selected CGCMs under the SRES-A1B scenario. The
9 rainband corresponding to the Baiu rainband is located from southern China to Japan in the
10 MME-CGCM (Fig. 3a). The MIROCM is similar to the MIROCH, but the amount of
11 precipitation in the MIRCOCM is much weaker than that in the MIROCH (Figs. 3g and 3h),
12 which depends on their resolutions [*Kawatani and Takahashi, 2003*]. Most CGCMs do not
13 simulate the Baiu rainbands clearly (Figs. 3b-3g), but only the MIROCH does (Fig. 3h).
14 Some CGCMs could not accurately simulate the Baiu rainband in the present climate
15 (figure not shown), resulting in the obscure Baiu rainband in the future climate.
16 Considering that we selected the CGCMs with higher performance in East Asia from the

1 CMIP3 multi-model dataset, the other CGCMs simulate the Baiu rainbands more poorly.

2

3 Figure 4 shows the differences in the 30-year mean June precipitation between the
4 20C3M for the present climate (1970-1999) and the SRES-A1B scenario for the future
5 climate (2060-2089). The MME-CGCM indicates an increase in precipitation over mid-
6 and high-latitude regions, especially near the Baiu rainband, and a decrease in precipitation
7 over the low-latitude region (Fig. 4a). The change in precipitation of the MME-CGCM is,
8 however, quite different from the changes in the individual CGCMs. The GFDL and the
9 MRI show a decrease in precipitation (Figs. 4c and 4e), while the CCCMA, MIROCM, and
10 MIROCH show an increase in precipitation over Japan. Only the INGV shows a decrease
11 in precipitation over Northern China (Fig. 4d). The MIROCH and the MIROCM project
12 similar changes in precipitation except for the amount (Figs. 4g and 4h).

13

14

1 3. Procedure of a Pseudo-Global Warming Downscaling Method

2 A control run was conducted to simulate the Baiu rainband in the control period,
3 which is the 1990s in this paper. We used the Advanced Research of Weather Research and
4 Forecasting (WRF) model version 2.2 [Skamarock *et al.*, 2005]. The ERA40 data was
5 applied to the initial and boundary conditions of the WRF model (CTRL-ERA40 run). The
6 specifications of the numerical simulations are summarized in Table 2. The model domain
7 was covered by 300 x 200 grids with 20-km grid intervals (Fig. 1). The simulation was
8 executed from May 22 to July 1 for each year. The first ten-day period was defined as a
9 spin-up duration. Physical processes of the surface-layer, boundary-layer, and land surface
10 were calculated by the Monin-Obukhov (Janjic Eta) scheme [Janjic, 1996], the
11 Mellor-Yamada-Janjic (Eta) TKE scheme [Janjic, 2002], and the Noah land surface
12 scheme [Chen and Dudhia, 2001], respectively. Both the Kain-Fritsch convective
13 parameterization scheme [Kain and Fritsch, 1993] and the WRF single-moment
14 microphysics scheme (WSM6) [Hong and Lim, 2006] were activated as the precipitation
15 process.

16

1 Next, the present climatic fields, including the wind, temperature, geopotential
2 height, surface pressure, and sea surface temperature, were calculated by the 30-year
3 monthly mean from 1970 to 1999 in the 20C3M, as in Section 2. Here, we used one
4 ensemble member in each CGCM. The future climatic fields were calculated by the
5 30-year monthly mean from 2060 to 2089 under the SRES-A1B scenario. The
6 pseudo-future six-hourly dataset was obtained by adding the components of the climatic
7 change between the present and future climates into the six-hourly ERA40 data in the
8 1990s. The climate of the pseudo-future dataset corresponds to the future climate
9 (2060-2089), while the variability, such as short-term disturbances and interannual
10 variability, is similar to that in the 1990s. The PGW-DS runs were conducted using the
11 pseudo-future six-hourly data. The flow chart of the PGW-DS is summarized in Fig. 5.

12

13 The relative humidity of the future climate was assumed to be equal to that of the
14 present climate, which means that the absolute amount of water vapor was expected to
15 increase due to global warming because the saturation vapor pressure increases with
16 temperature (i.e., the Clausius-Clapeyron relation). It has often been suggested that the

1 distribution of relative humidity should remain roughly constant in the warming climate
2 because the global trend of near-surface relative humidity is very small during recent
3 decades [Dai, 2006; Trenberth, 2005] and there is no detectable trend in relative humidity
4 in the upper troposphere [Soden *et al.*, 2005].

5

6 We conducted seven PGW-DS runs using the seven CGCMs selected in Section 2,
7 i.e., the PGW-CCCMA, PGW-CNRM, PGW-INGV, PGW-GFDL, PGW-MIROCM,
8 PGW-MIROCH, and PGW-MRI runs. In addition, another PGW-DS run, called the
9 PGW-MME run, was conducted using the MME-CGCM. We estimated future climatic
10 changes in the Baiu rainband with a comparison of the CTRL-ERA40 run with the seven
11 PGW-DS runs and the PGW-MME run.

12

13 Considering the linear approximation, the pseudo-future six-hourly data satisfies the
14 hydrostatic equilibrium, the equation of continuity, and the linear terms of dynamical
15 equations. On the other hand, the balance of nonlinear terms, such as an advection term, is
16 slightly disrupted. The PGW-DS applies the pseudo-future six-hourly data to only the

1 initial and lateral boundary conditions. The imbalanced error caused by the nonlinear term
2 seems to be smaller than the imbalanced errors between the lateral boundary conditions
3 and interior mesh values.

4

5 A simple numerical experiment was also conducted to investigate the impact of only
6 the temperature rise on the Baiu rainband (TEMP-RISE run), as in *Frei et al.* [1998]. The
7 initial and boundary conditions were provided by the six-hourly ERA40 data in the 1990s,
8 but 3K in atmospheric temperature at all vertical levels and 2.2K at the sea surface
9 temperature were added; these were comparable to the temperature rise at lower
10 atmospheric levels and the sea surface in the MME-CGCM at the end of 21st Century
11 under the SRES-A1B scenario, respectively. The geopotential height was recalculated
12 according to the temperature rise.

13

1 4. Results of Downscalings

2 4.1 Observations and Control Run

3 Figure 6a shows the distributions of the 10-year mean precipitation in June during
4 the 1990s observed by *in situ* stations provided by the China Meteorological
5 Administration in China and Automated Meteorological Data Acquisition System
6 (AMeDAS) provided by JMA in Japan. Heavy precipitation exceeding 420 mm/month is
7 observed over the south of the Yangtze River basin (28°N, 118°E) and around the southern
8 coast of China. A large amount of precipitation is also observed over Kyushu in Japan. The
9 amount of precipitation drastically decreases to the north of the Yangtze River. Figure 6b
10 shows the distribution of the 10-year mean precipitation derived from CMAP. The Baiu
11 rainband extends from southern China to Japan.

12
13 The CTRL-ERA40 run accurately simulates the Baiu rainband extending from
14 southern China to Japan and the distribution of precipitation in China, e.g., a large amount
15 of precipitation over the south of the Yangtze River basin and the southern coast of China,
16 and a drastic decrease in precipitation to the north of the Yangtze River (Fig. 6c). Some

1 previous studies focused on the regional climate modeling without interior or spectral
2 nudging [e.g., *Castro et al.*, 2005]. The climatic fields of wind and geopotential height
3 simulated by the CTRL-ERA40 run without interior or spectral nudging have some small
4 differences from the original ERA40 data. The CTRL-ERA40 run, however, well simulates
5 the location and strength of the Baiu rainband in the 1990s, as shown in Fig. 6, which
6 makes it possible to estimate future changes in the Baiu rainband. It should be noted that
7 the amount of precipitation is overestimated, especially around the center of southern
8 China (25°N, 118°E).

9

10 4.2 PGW-DS runs

11 The Baiu rainbands can be simulated from southern China to Japan in all PGW-DS
12 runs as strongly as in the CTRL-ERA40 run (Fig. 7). Most PGW-DS runs shows that the
13 amount of precipitation increases over the southern parts of the Baiu rainband but
14 decreases over the northern parts of the Baiu rainband (Figs.7 and 8). This feature is
15 strongly simulated by the PGW-INGV run (Fig. 8d) but is not clear in the PGW-MIROCH
16 and PGW-MIROCM runs in which precipitation increases over the Baiu rainband (Figs. 8g

1 and 8h).

2

3 Figure 9 shows the interannual variability of the regional mean precipitation in June
4 over Region B shown in Fig. 1. Region B is wide enough for almost of the precipitation
5 around the Baiu rainband to be detected. The amounts of precipitation simulated by the
6 PGW-MME and PGW-DS runs are 10 - 50 mm/month larger than that simulated by the
7 CTRL-ERA40 run. The PGW-MME and individual PGW-DS runs show similar
8 interannual variability to the CTRL-ERA40 run. The PGW-MIROCH, however, simulated
9 more precipitation than the other PGW-DS runs in 1993 and 1997. The PGW-INGV also
10 simulated more precipitation in 1991 and 1993. It is noteworthy that the average of the
11 seven PGW-DS runs (hereafter, MME-PGW-DS) shows quite similar interannual
12 variability to the PGW-MME run.

13

14 Figure 10 shows the latitudinal distributions of the zonal mean precipitation, which
15 is averaged every 2.5 degrees over Region B, in June during the 1990s and pseudo warmed
16 1990s. The maximum precipitation of about 280 mm/month, which signals the peak of the

1 Baiu rainband, appears at around 27.5°N - 30°N in the CTRL-ERA40 run. On the other
2 hand, the maxima appear at around 25°N - 27.5°N in the PGW-MME run and most
3 PGW-DS runs. The precipitation increases over the southern part of the control Baiu
4 rainband simulated by the CTRL-ERA40 run (20°N - 27.5°N). Only the PGW-MIROCM
5 and PGW-MIROCH runs show an increase in precipitation over the control Baiu rainband.
6 The MME-PGW-DS shows quite a similar change to the PGW-MME run as well as the
7 interannual variability of the regional mean precipitation (Fig. 9).

8

9 4.3 Comparison between PGW-DS runs and CGCMs

10 We compare the inter-model variability in the change of precipitation simulated by
11 the PGW-DS runs (Figs. 7 and 8) and projections of the CGCMs (Figs. 3 and 4) with the
12 aid of the Taylor diagram [Taylor, 2001]. The observational data are applied to the
13 reference data in the original Taylor diagram (see Section 2, Fig. 2), while the
14 MME-CGCM and the MME-PGW-DS are applied to the reference data here. We call this
15 Taylor diagram the “MME Taylor diagram.” It should be noted that the MME Taylor
16 diagram cannot be used to evaluate the performances of the models in the future climate.

1 The skill score, which shows the skill of CGCM in the original Taylor diagram, refers to
2 the similarity among the models and the MME mean in the MME Taylor diagram. The skill
3 score is called a “similarity score” in the MME Taylor diagram. The models with high
4 (low) similarity scores show similar features to (different features from) the MME mean.
5 When all models have high (low) similarity scores, the inter-model variability is small
6 (large). When the variance of the MME mean is much smaller than those of the individual
7 models, all models have different features.

8
9 Figure 11 shows the MME Taylor diagrams for the spatial distribution of
10 precipitation in the future climate (11a and 11c) and the difference in precipitation among
11 the present and future climates (11b and 11d). Figures 11a and 11b show the projections of
12 the CGCMs and Figs. 11c and 11d show the results of the PGW-DS runs. Figures 11a, 11b,
13 11c, and 11d correspond to Figs. 3, 4, 7, and 8, respectively. The similarity scores for the
14 precipitation in the CGCMs are lower than 0.7 (Fig. 11a). The CCCMA, MIROCH, and
15 MRI have smaller similarity scores than the other models, which indicates that their
16 projections are far from the MME-CGCM. The location of the rainband in the CCCMA is

1 quite different from that in the MME-CGCM (Figs. 3a and 3b), which results in the lowest
2 correlation coefficient and the smallest similarity scores. The variances in the MIROCH
3 and the MRI are higher than those of the others depending on the amount of precipitation
4 around the rainband (Figs. 3e and 3h). The similarity scores for the change in precipitation
5 are quite low in all CGCMs (Fig. 11b). They are lower than 0.2 except for the MIROCM
6 and the CNRM. The variance of the MME-CGCM is much smaller than those of the seven
7 CGCMs. These results indicate that the seven CGCMs show different changes in the
8 spatial distribution of precipitation, i.e., different changes in the Baiu rainband.

9

10 On the other hand, all PGW-DS runs show much higher similarity scores than the
11 CGCMs. Their correlation coefficients exceed 0.90 in most PGW-DS runs (Fig. 11c). The
12 variances of all PGW-DS runs are comparable to that of the MME-PGW-DS. Even the
13 PGW-MIROCH, PGW-MRI, and PGW-CCCMA show high similarity scores, although
14 their original CGCMs, i.e., MIROCH, MRI, and CCCMA, show quite low similarity
15 scores (Fig. 11a). Figure 11c indicates that all PGW-DS runs simulate similar locations and
16 strengths for the Baiu rainband. Moreover, it is noteworthy that the PGW-MME run, which

1 is the PGW-DS run using the MME-CGCM, also shows a high similarity score of about
2 0.96. The similarity scores for the difference in precipitation in the PGW-DS runs are also
3 much higher than those in the CGCMs (Fig. 11d). They exceed 0.4, except for
4 PGW-MIROCH and PGW-MIROCM. As in Fig. 11c, the PGW-MME run shows a high
5 similarity score of about 0.73. The variances of the PGW-DS runs are comparable to that of
6 the PGW-MME run, except for the PGW-INGV run. The clear contrast of the decrease and
7 increase of precipitation results in the large variance in the PGW-INGV run (Fig. 8d). The
8 PGW-MIROCM and PGW-MIROCH runs have low correlation coefficients and low
9 similarity scores because they simulate different changes in the spatial distribution of
10 precipitation compared with the other PGW-DS runs and the PGW-MME run (Fig. 8).
11 Figure 11 suggests that the PGW-DS runs decrease the inter-model variability in the Baiu
12 rainband relative to the original CGCMs.

13

14

1 5. Discussion

2 A significant assumption of the PGW-DS is the neglect of changes in variability,
3 such as interannual variability, in the future climate. The future changes in the amplitudes
4 of the interannual variability obtained by selected CGCMs and their uncertainty were
5 investigated in regard to the geopotential height at three pressure levels (850 hPa, 500 hPa,
6 and 200 hPa) over Region B shown in Fig. 1. We estimated the difference in the standard
7 deviation of interannual variability (hereafter, DSDIV) between the present climate
8 (1970-1999) and the future climate (2060-2089) simulated by each CGCM as well as the
9 DSDIV between ERA40 data and each CGCM in the present climate. The DSDIVs
10 between the present and the future climates were comparable to those between ERA40 data
11 and the individual CGCMs in the present climate at all of three pressure levels. These facts
12 indicate that the uncertainty of CGCMs is too large to discuss the change in the amplitudes
13 of the interannual variability. In addition, the mean of the DSDIVs between the present and
14 future climates among the CGCMs was much smaller than the standard deviation of the
15 DSDIVs among the CGCMs. These results suggest that the signal of the change in the
16 amplitudes of the interannual variability is insignificant in the CGCMs.

1

2 The PGW-DS based on other decades, such as the 1970s and the 1980s, may
3 simulate the different changes in the Baiu rainband from those simulated by the PGW-DS
4 based on the 1990s. We conducted the additional control run (hereafter, CTRL-ERA40-80s
5 run) and the PGW-MME run (hereafter, PGW-MME-80s run) in the 1980s. Here, the
6 PGW-MME-80s run is expected to represent the average of all PGW-DS runs using
7 individual CGCMs in the 1980s (see Figs. 9 and 10).

8

9 The CTRL-ERA40-80s simulates the Baiu rainband extending from southern China
10 to Japan (Fig. 12a). In comparison with the 1990s, the location of the Baiu rainband is
11 similar to that in the 1990s, while the amount of precipitation is smaller than that in the
12 1990s, which is also shown in observational data (figure not shown). Figure 12b shows the
13 difference in precipitation in the CTRL-ERA40-80s and PGW-MME-80s runs.
14 Precipitation increases over the southern part of the control Baiu rainband, which suggests
15 the southward shift of the Baiu rainband. It is noteworthy that the change in the Baiu
16 rainband simulated by the PGW-MME-80s run is quite similar to the PGW-MME run

1 based on the 1990s (Fig. 8a). In consideration with the mechanism to form the Baiu
2 rainband, it is unlikely that the Baiu rainband locates at a quite different place in the other
3 present decades. The results suggest that the PGW-DS is expected to obtain similar results
4 regardless of the selected decade.

5

6 These facts also suggest that the selection of reanalysis data, such as ERA40 data,
7 the National Centers for Environmental Prediction / National Center for Atmospheric
8 Research (NCEP/NCAR) reanalysis data, and Japanese 25-year Reanalysis (JRA25) data,
9 would not affect the results of the PGW-DS run. The differences in the reanalysis data are
10 much smaller than those between decades, e.g., the 1980s and the 1990s.

11

12 An increase in temperature due to global warming would contribute to the change in
13 the Baiu rainband because of the increase of the saturation vapor pressure. The PGW-DS
14 assumes that the relative humidity of the future climate would be equal to that of the
15 present climate, which results in an increase in the absolute value of water vapor in the
16 warm future climate following the Clausius-Clapeyron relationships. The impact of a

1 temperature rise on the Baiu rainband is estimated by the TEMP-RISE run assuming only
2 an atmospheric and sea surface temperature rise (see Section 3).

3

4 The black broken lines in Figs. 9 and 10 show the results of the TEMP-RISE run.

5 The regional mean precipitation increases, as in the PGW-DS runs (Fig. 9), while the

6 amount of precipitation increases at almost the same rate at all latitudes (Fig. 10). The

7 southward shift of the Baiu rainband, which is shown in most PGW-DS runs, is not

8 simulated by the TEMP-RISE run. The TEMP-RISE run suggests that the temperature rise

9 would contribute to the increase of precipitation around the Baiu rainband, while the other

10 factors of the PGW-DS runs would influence the shift of the Baiu rainband. It must be

11 noted that we only indicated the direct effect of the temperature rise in the regional scale

12 shown in Fig. 1 without considering the indirect effect accompanied with the SST rise,

13 such as the global-scale atmospheric response to the El Nino conditions of the ocean

14 pointed out in previous studies [e.g. *Kitoh et al.*, 2005].

15

16 The change in the location of the Baiu rainband is thought to be affected by the

1 change in the large-scale circulation projected by the CGCMs throughout the lateral
2 boundary of the RCM. *Ninomiya* [2000] suggested that the differential advection of the
3 equivalent potential temperature, which consists of a poleward moisture flux by the
4 low-level jet and cold air advection by the upper-level jet, is a primary factor in the
5 formation of the active Baiu rainband. *Yoshikane et al.* [2001] reported that the Baiu
6 rainband is quite sensitive to the positions of the upper-level jet and the low-level jet. It is
7 suggested that the future change in summer precipitation in East Asia will be attributable to
8 the change in the lower moisture flux and its convergence associated with the subtropical
9 high [*Kurihara et al.*, 2005].

10

11 Figure 13 shows the difference of the moisture flux at 850 hPa between the
12 CTRL-ERA40 run and the PGW-MME run. Contour lines represent the zero vorticity at
13 200 hPa, which mean the axes of the upper-level jet. The poleward moisture flux increases
14 around the southwestern boundary of the model domain (15°N , 115°E). The eastward to
15 northeastward moisture flux also increases over the northeastern Pacific Ocean (115°E - 1
16 45°E , 20°N - 30°N). The increase of the lower-level moisture flux enhances the convective

1 instability, resulting in more precipitation around the Baiu rainband in the PGW-MME run
2 than that in the CTRL-ERA40 run. On the other hand, the zero vorticity contour line shifts
3 southward (110-140°E), which means that the meandering of the upper-level jet is more
4 remarkable in the PGW-MME run than that in the CTRL-ERA40 run. The larger amplitude
5 of the meandering brings cold air more southward in the upper level. It can be summarized
6 that the enhancement and the southward shift of the Baiu rainband are the results of the
7 change in the differential advection of equivalent potential temperature caused by two
8 factors: (1) the increase of the northeastward moisture flux over the northwestern Pacific
9 Ocean at the lower level, and (2) the increase of the southward cold air advection in the
10 upper level. However, detailed mechanisms in the shift of the Baiu rainband are still
11 unknown. Further studies are needed to identify them.

12

13 One major problem is the projection of typhoons in the future climate that would
14 sometimes strongly affect the amount of precipitation during the Baiu season. The
15 PGW-DS may not estimate the impact of a typhoon accurately because of the assumption
16 of PGW-DS on the boundary conditions. To reduce the uncertain impacts of a typhoon, this

1 study focuses on only June, when there are fewer typhoons than in the other months. Since
2 several typhoons annually approach Japan and China from July to September, extreme care
3 must be exercised regarding typhoons when the PGW-DS is conducted in such months.
4 *Knutson et al.* [2008] applied a similar method to the simulation of the Atlantic hurricane
5 frequency using a wide domain for the RCM. The PGW-DS would require a much larger
6 domain than has been assumed here when the PGW-DS estimates the change in the Baiu
7 rainband, including the impact of typhoons.

8

9 The PGW-DS assumes unchanged interannual variability and frequencies of
10 disturbances. The change in extreme precipitation events might be affected by them. The
11 usefulness of PGW-DS for extreme events should be examined in future works. We also
12 assume constant relative humidity between the present and future climates. Rowell and
13 Jooones [2005] suggested that the relative humidity tends to decrease over land in global
14 warming condition due to the change in large-scale land-sea circulation. The change in the
15 relative humidity in the regional scale would affect the amount and distribution of
16 precipitation. It is necessary to conduct further PGW-DSs to investigate the impact of the

1 change in the relative humidity.

2

3 The PGW-DS has some limitations in the assessment of future projections. However,

4 the PGW-DS can reduce the inter-model variability of changes in the Baiu rainband and

5 contribute to the reduction of uncertainty in the climate changes projected by multiple

6 CGCMs.

7

1 6. Conclusion

2 For the estimation of the change in the Baiu rainband due to global warming,
3 multiple PGW-DS runs were conducted using selected CMIP3 multi-model dataset giving
4 better performance around East Asia in June. Most PGW-DS runs and the PGW-MME run,
5 which is the PGW-DS run using the multi-CGCM ensemble mean, simulated an increase in
6 precipitation over the Baiu rainband and the southward shift of the Baiu rainband. The
7 PGW-MME run has good similarity to the average of all PGW-DS runs, e.g., the change in
8 the regional mean precipitation and the shift of the Baiu rainband. These facts suggest that
9 the average of the multi-PGW-DS runs can be replaced by a single PGW-DS using the
10 multi-CGCM ensemble mean, which significantly reduces the computational expense. The
11 PGW-MME run based on the 1980s simulated the change in the Baiu rainband with
12 considerable similarity to the PGW-MME run based on the 1990s, suggesting that the
13 PGW-DS is expected to obtain similar results regardless of the selection of control decade.
14 The comparison of the PGW-DS runs and the CGCM projections suggests that the
15 PGW-DS runs reduce the inter-model variability in the Baiu rainband caused by CGCMs
16 themselves. Although the PGW-DS assumes an unchanged variability in the future climate,

- 1 the PGW-DS can be used as a new method to assess the regional climate changes due to
- 2 global warming.
- 3

1 Acknowledgments

2 This work was supported by the Global Environment Research Fund (B-061) of the
3 Ministry of the Environment and Ministry of Education, Culture, Sports, Science, and
4 Technology (MEXT), Japan. The authors (Drs. Ueda, Inoue, and Kimura) were supported
5 by the Global Environment Research Fund (S-5-2 and S-5-3) of the Ministry of the
6 Environment Japan in the course of this work. We acknowledge the modeling groups, the
7 Program for Climate Model Diagnosis and Intercomparison (PCMDI), and the WCRP's
8 Working Group on Coupled Modelling (WGCM) for their roles in making the WCRP
9 CMIP3 multi-model dataset available. Support of this dataset was provided by the Office
10 of Science, U.S. Department of Energy. This work was jointly supported by the China
11 National Key Planning Development for Basic Research (Grant No. G1999043405). We
12 appreciate Dr. Takayabu in the Meteorological Research Institute for his helpful
13 suggestions. We also thank three anonymous reviewers for their precise and useful
14 comments.

15

1 References

- 2 Castro, C. L., R. A. Pielke Sr., and G. Leoncini (2005), Dynamical downscaling:
3 Assessment of value retained and added using the Regional Atmospheric Modeling
4 System (RAMS), *J. Geophys. Res.*, *110*, D05108, doi:10.1029/2004JD004721.
- 5 Chen, F., and J. Dudhia (2001), Coupling an advanced land-surface/hydrology model with
6 the Penn State/NCAR MM5 modeling system. Part I: Model description and
7 implementation, *Mon. Weather Rev.*, *129*, 569-585.
- 8 Dai, A. (2006), Recent climatology, variability and trends in global surface humidity, *J.*
9 *Climate*, *19*, 3589–3606.
- 10 Frei, C., C. Schar, D. Luthi, and H. C. Davies (1998), Heavy precipitation processes in a
11 warmer climate, *Geophys. Res. Lett.*, *25*, 1431-1434.
- 12 Giorgi, F., and L. O. Mearns (2002), Calculation of average, uncertainty range, and
13 reliability of regional climate changes from AOGCM simulations via the "reliability
14 ensemble averaging"(REA) method, *J. Climate*, *15*, 1141-1158.
- 15 Hara, M., T. Yoshikane, H. Kawase, and F. Kimura (2008), Estimation of the impact of
16 global warming on snow depth in Japan by the Pseudo-Global-Warming method,

1 *Hydrological Research Letters*, 2, 61-64.

2 Hong, S.-Y., and J.-O. J. Lim (2006), The WRF single-moment microphysics scheme
3 (WSM6), *J. Korean Meteorol. Soc.*, 42, 129-151.

4 Inoue, T., and H. Ueda (2009), Evaluation for the seasonal evolution of the summer
5 monsoon over the Asian and western north Pacific sector in the WCRP CMIP3
6 Multi-model Experiments, *J. Meteor. Soc. Japan*, 87, 539-560.

7 IPCC (2000), Emissions Scenarios. A Special Report of Working Group II of the
8 Intergovernmental Panel on Climate Change. Cambridge University Press,
9 Cambridge.

10 IPCC (2001), Climate Change 2001: The Scientific Basis. Contribution of Working Group
11 I to the Third Assessment Report of the Intergovernmental Panel on Climate Change,
12 Houghton, J. T. et al. (eds.), Cambridge University Press, Cambridge, United
13 Kingdom and New York, USA, 881pp.

14 IPCC (2007), Climate Change 2007: The Physical Science Basis. Contribution of Working
15 Group I to the Fourth Assessment Report of the Intergovernmental Panel on Climate
16 Change, Solomon, S., D. Qin, M. Manning, Z. Chen, M. Marquis, K. B. Averyt, M.

- 1 Tignor, H. L. Miller, (eds.), Cambridge University Press, Cambridge, United
2 Kingdom and New York, USA, 996 pp.
- 3 Janjic, Z. I. (1996), The surface layer in the NCEP Eta Model. Preprints, *11th Conf. on*
4 *Numerical Weather Prediction*, Norfolk, VA, Amer. Meteor. Soc., 354–356.
- 5 Janjic, Z. I. (2002), Nonsingular implementation of the Mellor-Yamada level 2.5 scheme in
6 the NCEP Meso model, *NCEP Office Note*, 437, 1-61.
- 7 Kain, J. S., and J. M. Fritsch (1993), Convective parameterization for mesoscale models:
8 The Kain-Fritsch scheme, *The Representation of Cumulus Convection in Numerical*
9 *Models, Meteor. Monogr.*, 46, Amer. Meteor. Soc., 165–170.
- 10 Kang, I. S., K. Jin, B. Wang, K. M. Lau, J. Shukla, V. Krishnamurthy, S. D. Schubert, D. E.
11 Waliser, W.F. Stern, A. Kitoh, G. A. Meehl, M. Kanamitsu, V. Y. Galin, V. Satyan, C.
12 K. Park, and Y. Liu (2002), Intercomparison of the climatological variations of Asian
13 summer monsoon precipitation simulated by 10 GCMs, *Clim. Dyn.*, 19, 383-395.
- 14 Kato, H., K. Nishizawa, H. Hirakuchi, S. Kadokura, N. Oshima, and F. Giorgi (2001),
15 Performance of RegCM2.5/NCAR-CSM nested system for the simulation of climate
16 change in East Asia caused by global warming, *J. Meteor. Soc. Japan*, 79, 99-121.

- 1 Kawase, H., T. Yoshikane, M. Hara, B. Ailikun, F. Kimura, and T. Yasunari (2008),
2 Downscaling of the climatic change in the Mei-yu rainband in East Asia by a pseudo
3 climate simulation method, *SOLA*, 4, 73-76.
- 4 Kawatani, Y., and M. Takahashi (2003), Simulation of the Baiu front in a high resolution
5 AGCM, *J. Meteor. Soc. Japan*, 81, 113-129.
- 6 Kimoto, M. (2005), Simulated change of the East Asian circulation under global warming
7 scenario, *Geophys. Res. Lett.*, 32, L16701, doi:10.1029/2005GL023383.
- 8 Kimoto, M., N. Yasutomi, C. Yokoyama, and S. Emori (2005), Projected changes in
9 precipitation characteristics around Japan under the global warming, *SOLA*, 1, 85-88.
- 10 Kimura, F., and A. Kitoh (2007), Downscaling by pseudo global warming method, *The*
11 *Final Report of ICCAP*, 43-46.
- 12 Kitoh, A., M. Hosaka, Y. Adachi, and K. Kamiguchi (2005), Future projections of
13 precipitation characteristics in East Asia simulated by the MRI CGCM2, *Advances in*
14 *Atmospheric Sciences*, 22, 467-478.
- 15 Kitoh, A., and T. Uchiyama (2006), Changes in onset and withdrawal of the East Asian
16 summer rainy season by multi-model global warming experiments, *J. Meteor. Soc.*

1 *Japan*, 84, 247-258.

2 Knutson, T. R., J. J. Sirutis, S. T. Garner, G. A. Vecchi, and I. M. Held (2008), Simulated
3 reduction in Atlantic hurricane frequency under twenty-first-century warming
4 conditions, *Nature Geoscience*, 1, 359-364.

5 Kurashima, A., and Y. Hiranuma (1971), *Synoptic and climatological study on the upper*
6 *moist tongue extending from Southeast Asia to East Asia water balance of monsoon*
7 *Asia*, edited by M. M. Yoshino, pp. 153-169, Univ. of Tokyo Press, Tokyo.

8 Kurihara, K., K. Ishihara, H. Sasaki, Y. Fukuyama, H. Saitou, I. Takayabu, K. Murazaki, Y.
9 Sato, S. Yukimoto, and A. Noda (2005), Projection of climate change over Japan due
10 to global warming by High-Resolution Regional Climate Model in MRI, *SOLA*, 1,
11 97-100.

12 Kusunoki, S., J. Yoshimura, H. Yoshimura, A. Noda, K. Oouchi, and R. Mizuta (2006),
13 Change of Baiu rain band in global warming projection by an atmospheric general
14 circulation model with a 20-km grid size, *J. Meteor. Soc. Japan*, 84, 581-611.

15 Meehl, G. A., C. Covey, T. Delworth, M. Latif, B. McAvaney, J. F. B. Mitchell, R. J.
16 Stouffer, and K. E. Taylor (2007), The WCRP CMIP3 multimodel dataset: A new era

1 in climate change research, *Bull. Amer. Meteor. Soc.*, 88, 1383–1394.

2 Min, S.-K., E.-H. Park, and W.-T. Kwon (2004), Future projections of East Asian climate
3 change from multi-AOGCM ensembles of IPCC SRES scenario simulations, *J.*
4 *Meteor. Soc. Japan*, 82, 1187-1211.

5 Mizuta, R., K. Oouchi, H. Yoshimura, A. Noda, K. Katayama, S. Yukimoto, M. Hosaka, S.
6 Kusunoki, H. Kawai, and M. Nakagawa (2006), 20-km-mesh global climate
7 simulations using JMA-GSM model-mean climate states, *J. Meteor. Soc. Japan*, 84,
8 165-185.

9 Ninomiya, K. (2000), Large- and meso- α -scale characteristics of Meiyu/Baiu Front
10 associated with intense rainfalls in 1-10 July 1991, *J. Meteor. Soc. Japan*, 78,
11 141-157.

12 Ninomiya, K., T. Nishimura, W. Ofuchi, T. Suzuki, and S. Matsumura (2002), Features of
13 the Baiu front simulated in an AGCM (T42L52), *J. Meteor. Soc. Japan*, 80, 697-716.

14 Rowell, D.P., and R.G. Jones (2006), Causes and uncertainty of future summer drying over
15 Europe, *Climate Dyn.*, 27, 281-299.

16 Skamarock, W. C., J. Dudhia, D. O. Gill, D. M. Barker, W. Wang, and J. G. Powers (2005),

- 1 A description of the Advanced Research WRF version 2, *NCAR Tech. Rep.* TN-468,
2 100 pp.
- 3 Sato, T., F. Kimura, and A. Kitoh (2007), Projection of global warming onto regional
4 precipitation over Mongolia using a regional climate model, *J. Hydrol.*, 333,
5 doi:10.1016/j.jhydrol.2006.07.023.
- 6 Soden, B. J., D. L. Jackson, V. Ramaswamy, D. Schwarzkopf and X. Huang (2005) The
7 radiative signature of upper tropospheric moistening, *Science*, 310, 841–844.
- 8 Taylor, K.E. (2001), Summarizing multiple aspects of model performance in a single
9 diagram, *J. Geophys. Res.*, 106, 7183-7192.
- 10 Trenberth, K. E (2005), The impact of climate change and variability on heavy
11 precipitation, floods, and droughts, *Encyclopedia of Hydrological Sciences*,
12 Anderson M. G. (eds). John Wiley & Sons Ltd.
- 13 Ueda, H., A. Iwai, K. Kuwako, and M. E. Hori (2006), Impact of anthropogenic forcing on
14 the Asian summer monsoon as simulated by eight GCMs, *Geophys. Res. Lett.*, 33,
15 L06703, doi:10.1029/2005GL025336.
- 16 Uppala, S.M, et al. (2005), The ERA-40 re-analysis, *Quart. J. Roy. Meteorol. Soc.*, 131,

1 2961-3012.

2 Wang, Y. Q., L. R. Leung, J. L. McGregor, D.-K. Lee, W.-C. Wang, Y. H. Ding, and F.

3 Kimura (2004), Regional climate modeling: Progress, challenges, and prospects, *J.*

4 *Meteor. Soc. Japan*, 82, 1599-1628.

5 Xie, P., and P. A. Arkin (1997), Global precipitation: A 17-year monthly analysis based on

6 gauge observation, satellite estimates, and numerical model outputs, *Bull. Amer.*

7 *Meteor. Soc.*, 78, 2539–2558.

8 Yasunaga, K., M. Yoshizaki, Y. Wakazuki, C. Muroi, K. Kurihara, A. Hashimoto, S.

9 Kanada, T. Kato, S. Kusunoki, K. Oouchi, H. Yoshimura, R. Mizuta, and A. Noda

10 (2006), Changes in the Baiu frontal activity in the future climate simulated by

11 super-high-resolution global and cloud-resolving regional climate models, *J. Meteor.*

12 *Soc. Japan*, 84, 199-220.

13 Yoshikane, T., F. Kimura, and S. Emori (2001), Numerical study on the Baiu Front genesis

14 by heating contrast between land and ocean, *J. Meteor. Soc. Japan*, 79, 671-686.

15 Yoshizaki, M., C. Muroi, S. Kanada, Y. Wakazuki, K. Yasunaga, A. Hashimoto, T. Kato, K.

16 Kurihara, A. Noda, and S. Kusunoki (2005), Changes of Baiu (Mei-yu) frontal

1 activity in the global warming climate simulated by a cloud-resolving
2 non-hydrostatic regional model, *SOLA, 1*, 25-28.

3

1 Table captions

2 Table 1. Fifteen CGCMs with the necessary atmospheric and surface variables, which are

3 available at the CMIP3 database, to conduct the PGW-DS.

4

5 Table 2. Specifications of the simulations.

6

7

1 Figure captions

2 Fig. 1: Geographical map of the analysis area. Enclosed areas drawn by black, red, and
3 blue lines represent the Model Domain, Region A, and Region B, respectively.

4

5 Fig. 2: Taylor diagram for the June climatological precipitation and 850hPa wind
6 (1980-1999) for East Asia. Large colored circles represent the seven selected models, and
7 small black circles represent the other models.

8

9 Fig. 3: Thirty-year mean precipitation in June from 2060 to 2089 simulated by seven
10 CGCMs and MME-CGCM under the SRES A1B scenario.

11

12 Fig. 4: Difference in the 30-year mean precipitation in June between the 20C3M and SRES
13 A1B scenario. Blue represents the increase of precipitation under the SRES-A1B scenario.

14

15 Fig. 5: Flow chart of the PGW-DS.

16

1 Fig. 6: Distributions of ten-year mean precipitation in June during the 1990s (a) observed
2 by *in situ* stations provided by the China Meteorological Administration in China and
3 AMeDAS provided by JMA in Japan, (b) derived from CMAP, and (c) simulated by the
4 CTRL-ERA40 run.

5

6 Fig. 7: Distributions of June precipitation simulated by the seven PGW-DS runs and the
7 PGW-MME run.

8

9 Fig. 8: Difference in June precipitation among the CTRL-ERA40 run and each PGW-DS
10 run. Blue indicates that the precipitation in the PGW-DS runs is larger than that in the
11 CTRL-ERA40 run. The enclosed area with a red solid line represents the heavy rainfall
12 area of over 350 mm/month to the east of 110°E simulated by the CTRL-ERA40 run.

13

14 Fig. 9: Time series of the regional mean precipitation in June over Region B shown in Fig.
15 1b. A thick black solid line represents the CTRL-ERA40 run. The thick red solid and
16 broken lines represent the PGW-MME run and the average of all PGW-DS runs,

1 respectively. The other thin colored lines represent the individual PGW-DS runs. The thin
2 black broken line represents the TEMP-RISE run.

3

4 Fig. 10: Latitudinal distribution of the ten-year mean precipitation in June averaged 90°E -
5 150°E and every 2.5 degrees. All lines are the same as those in Fig. 9.

6

7 Fig. 11: MME Taylor diagrams for the ten-year mean precipitation in June projected by (a)
8 the CGCMs and (c) the PGW-DS runs and changes in precipitation projected by (b) the
9 CGCMs and (d) the PGW-DS runs.

10

11 Fig. 12: Distribution of (a) June precipitation simulated by the CTRL-ERA40-80s run and
12 (b) difference in June precipitation between the CTRL-ERA40-80s run and the
13 PGW-MME-80s run. The enclosed area with a red solid line represents the heavy rainfall
14 area of over 350 mm/month to the east of 110°E simulated by the CTRL-ERA40-80s run.

15

16 Fig. 13: Difference of the moisture flux at 850 hPa between the CTRL-ERA40 run and the

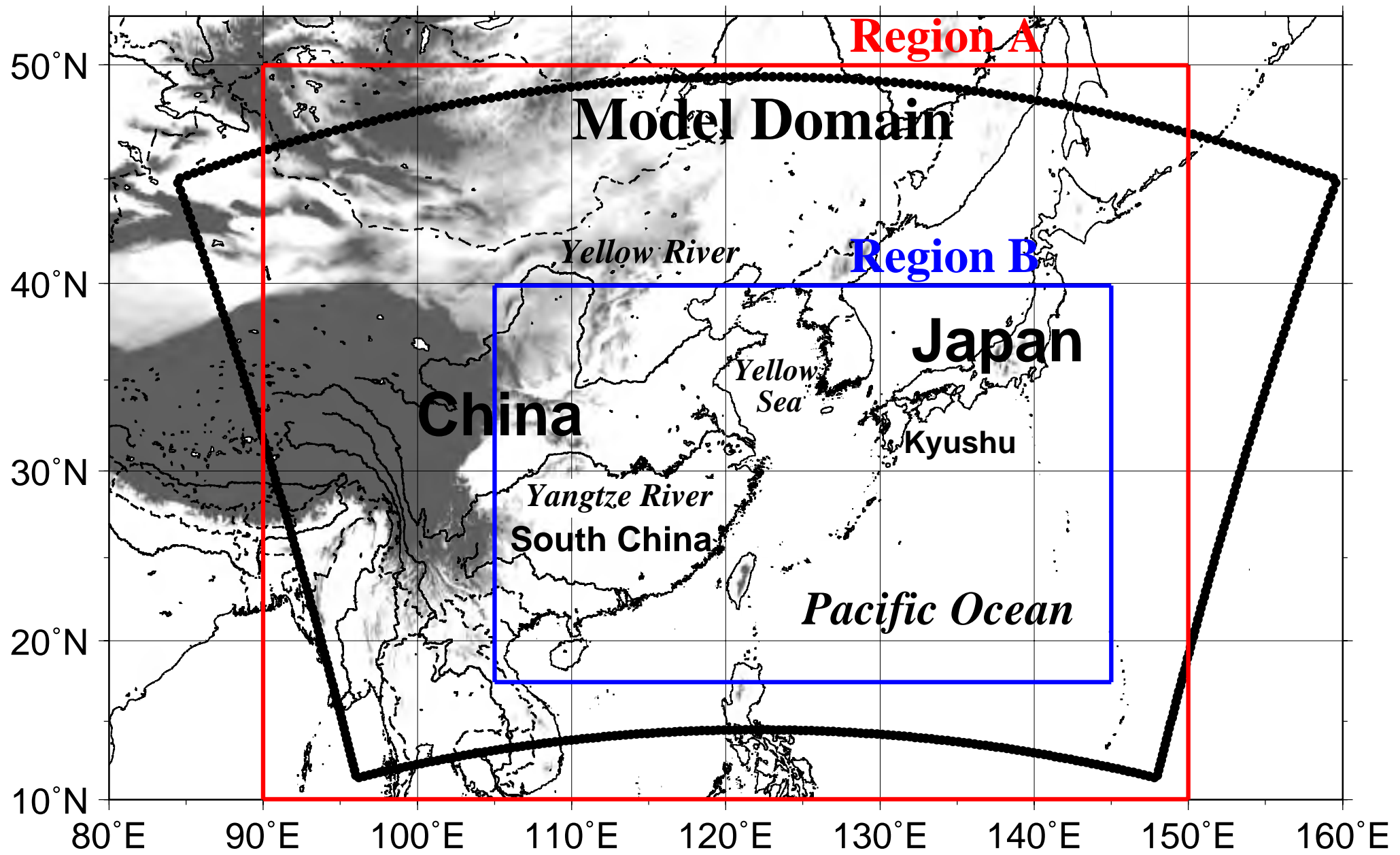
1 PGW-MME run (vector) and the zero vorticity contours at 200 hPa simulated by the
2 CTRL-ERA40 (bold broken line) and PGW-MME runs (bold solid line) in June. The gray
3 shading represents that the amount of precipitation in the PGW-MME run is 40 mm larger
4 than that in the CTRL-ERA40 run.
5

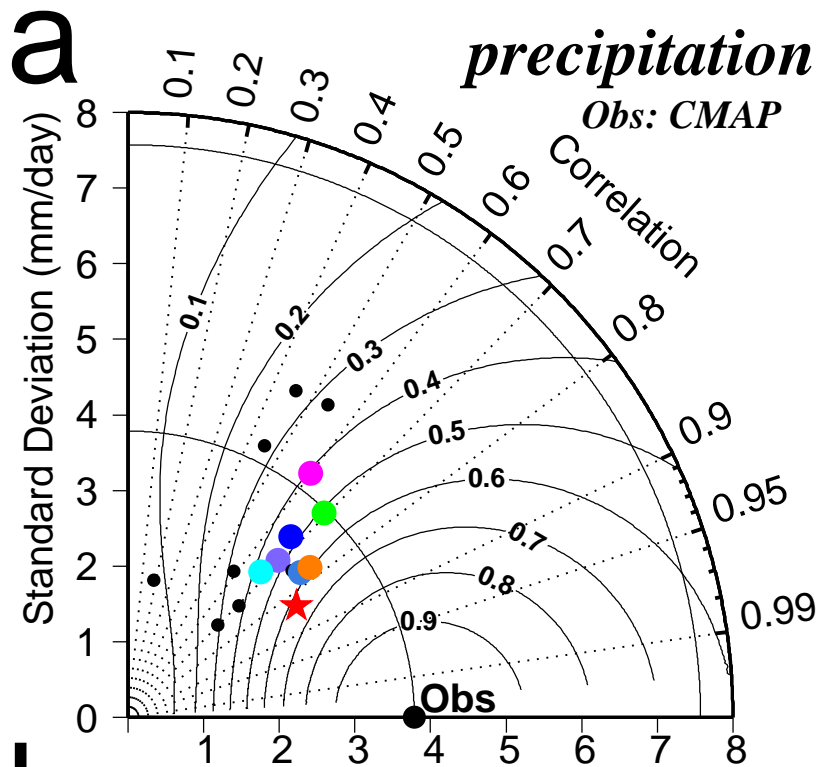
Table 1. Fifteen CMIP3 multi-model dataset having enough atmospheric variables to conduct the PGW-DS.

MODEL NAME in this paper	CMIP3 I.D.	Originating Group(s)	Country
CCCMA	CGCM3.1(T47)	Canadian Centre for Climate Modelling and Analysis	Canada
CCSM	CCSM3	National Center for Atmospheric Research	USA
CNRM	CNRM-CM3	Meteo-France, Centre National de Recherches Meteorologiques	France
GFDL20	GFDL-CM2.0	US Dept. of Commerce, NOAA	USA
GFDL21	GFDL-CM2.1	Geophysical Fluid Dynamics Laboratory	USA
GISS-EH	GISS-EH	NASA/Goddard Institute for Space Studies	USA
GISS-ER	GISS-ER		
IAP	FGOALS-g1.0	LASG/Institute of Atmospheric Physics	China
INGV	INGV-SXG	Instituto Nazionale di Geofisica e Vulcanologia	Italy
INM	INM-CM3.0	Institute for Numerical Mathematics	Russia
IPSL	IPSL-CM4	Institut Pierre Simon Laplace	France
MIROCH	MIROC3.2(hires)	Center for Climate System Research (The University of Tokyo), National Institute for Environmental Studies, and Frontier Research Center for Global Change (JAMSTEC)	Japan
MIROCM	MIROC3.2(medres)		
MRI	MRI-CGCM2.3.2	Meteorological Research Institute	Japan
PCM	PCM	National Center for Atmospheric Research	USA

Table 2. Specifications of the simulations.

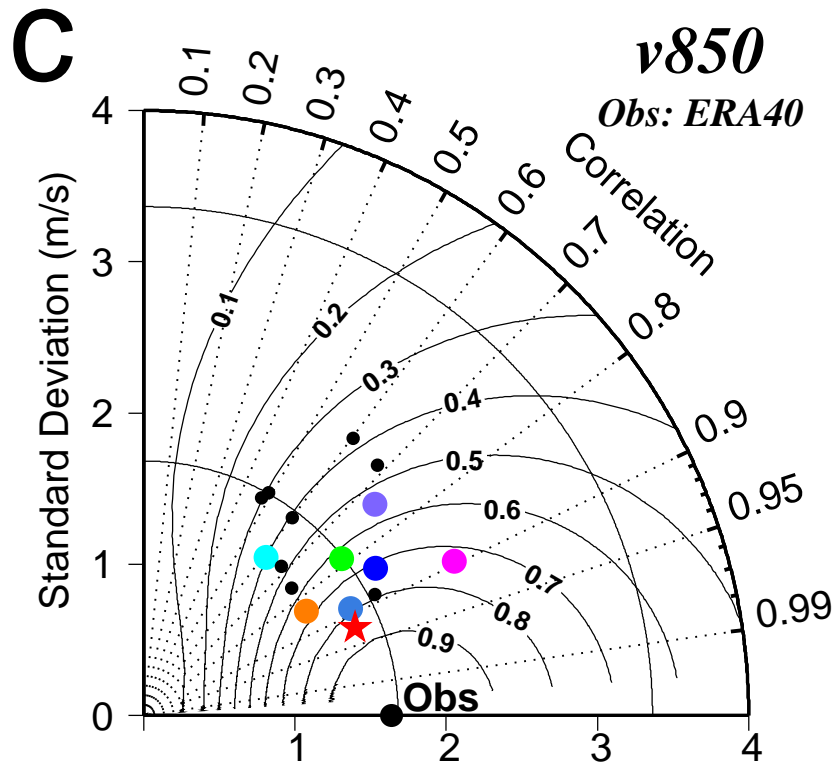
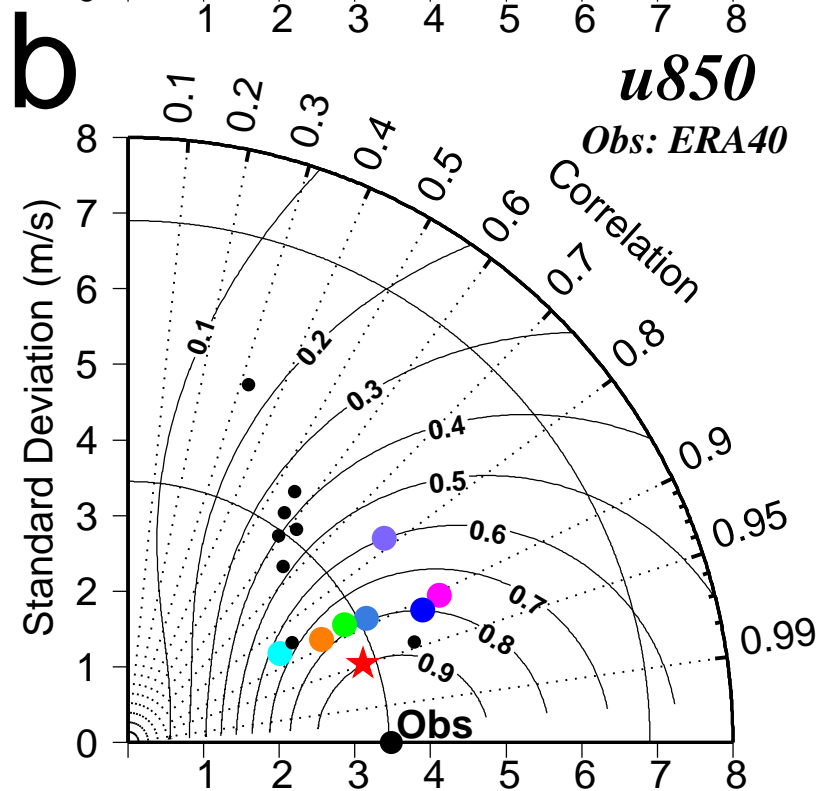
Run Name	Initial and boundary conditions	Based years
CTRL-ERA40	ERA40	1990s
PGW-MIROCM	ERA40+diff_MIROCM	1990s
PGW-MIROCH	ERA40+diff_MIROCH	1990s
PGW-MRI	ERA40+diff_MRI	1990s
PGW-GFDL	ERA40+diff_GFDL21	1990s
PGW-CNRM	ERA40+diff_CNRM	1990s
PGW-CCCMA	ERA40+diff_CCCMA	1990s
PGW-INGV	ERA40+diff_INGV	1990s
PGW-MME	ERA40+diff_MME-CGCM	1990s
PGW-MME-80s	ERA40+diff_MME-CGCM	1980s
CTRL-ERA40-80s	ERA40	1980s
TEMP-RISE	ERA40+ATM3.0K_SST2.2K	1990s

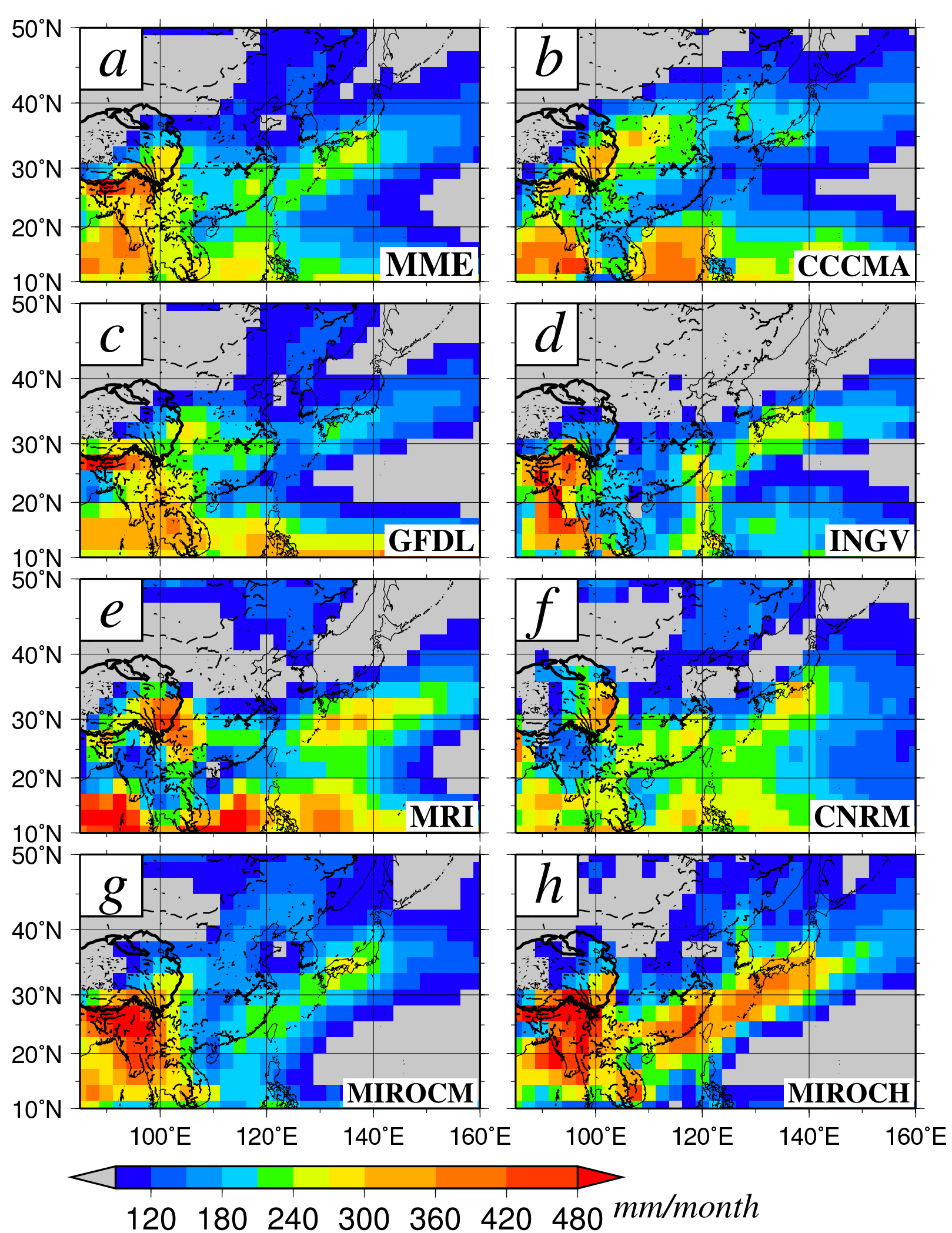


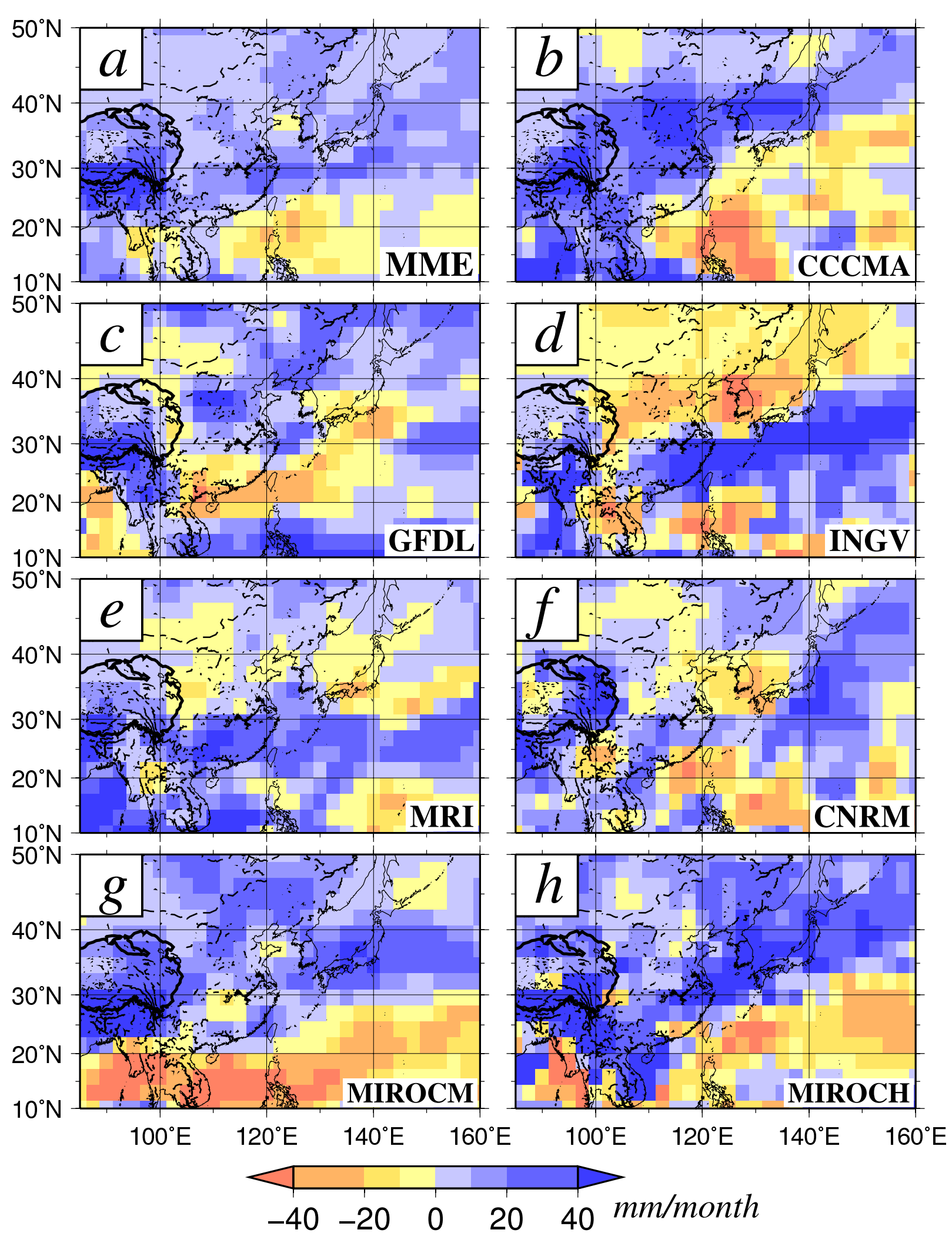


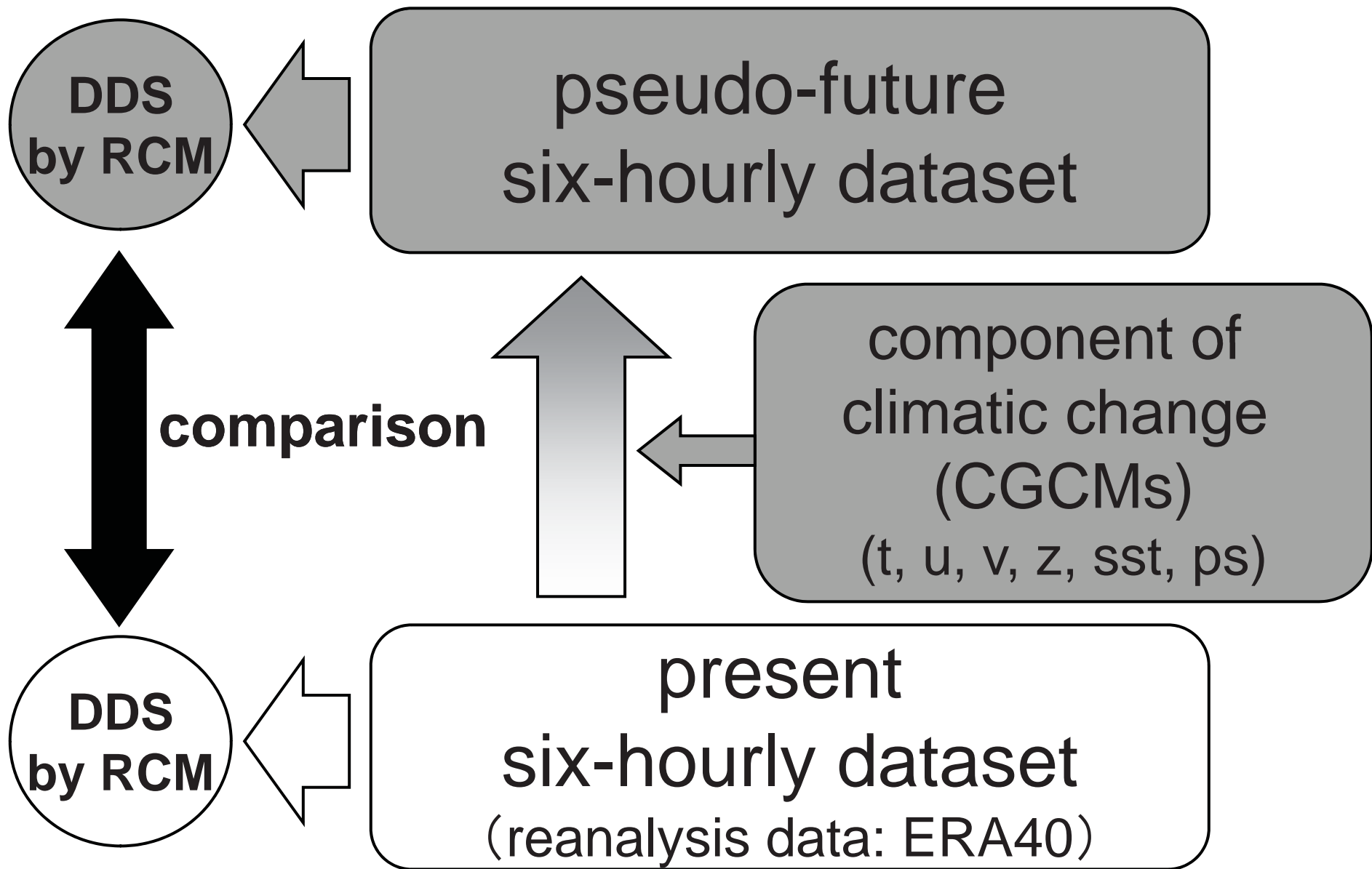
Taylor diagram

- CCCMA
- CNRM
- GFDL21
- INGV
- MIROCH
- MIROCM
- MRI
- ★ MME-CGCM

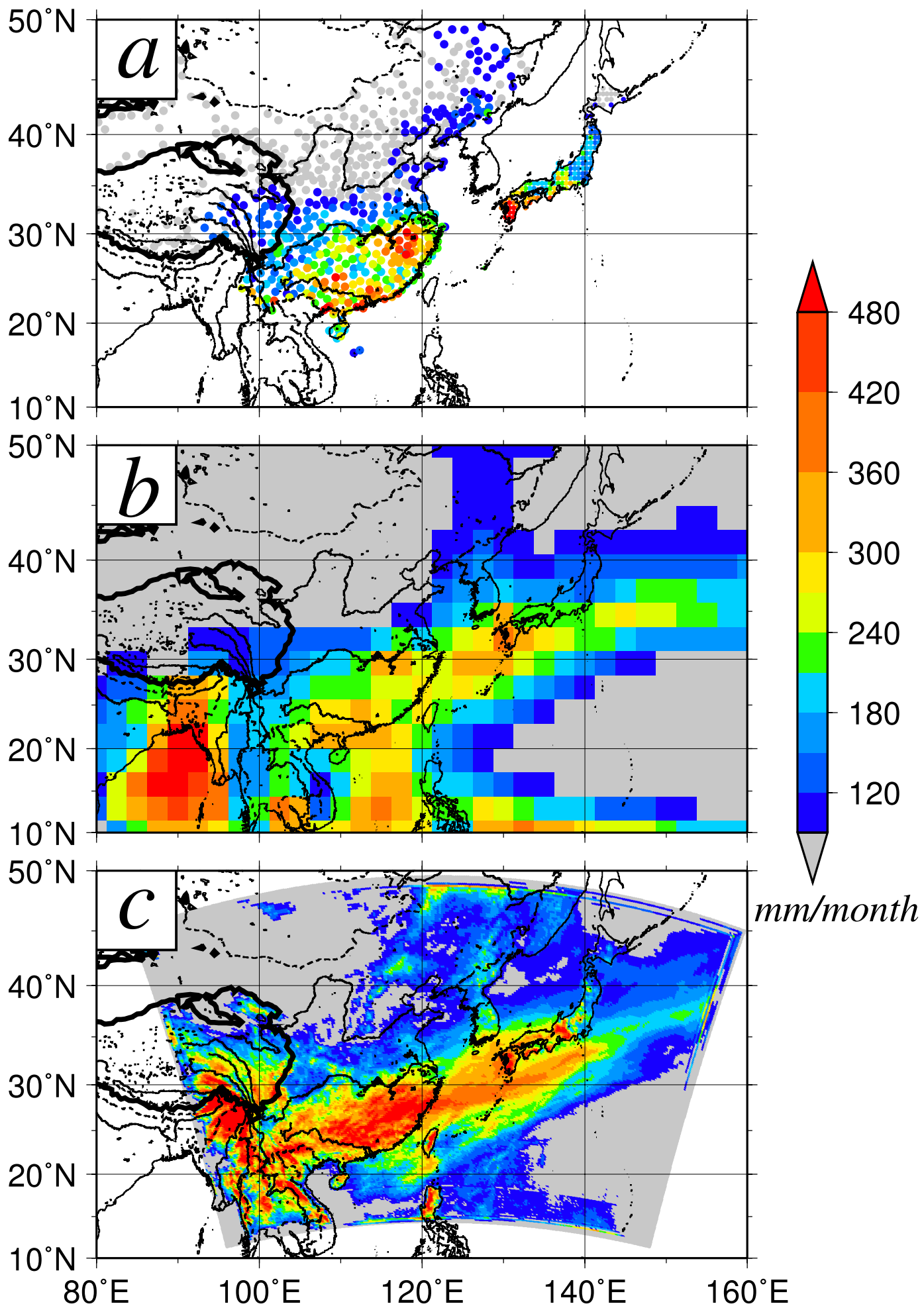


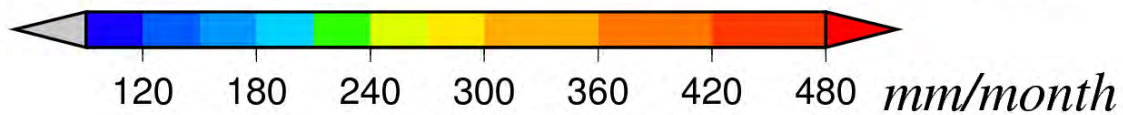
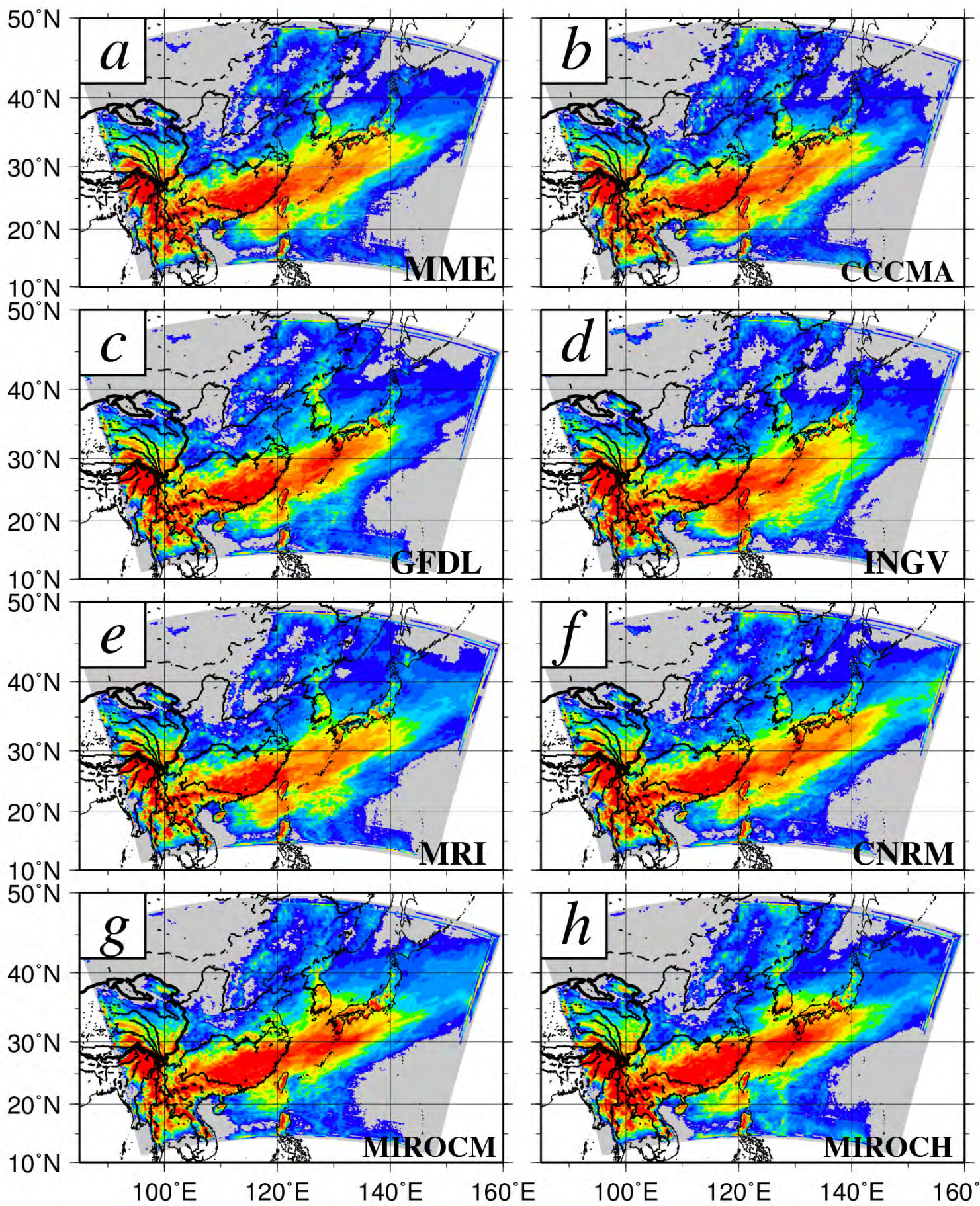


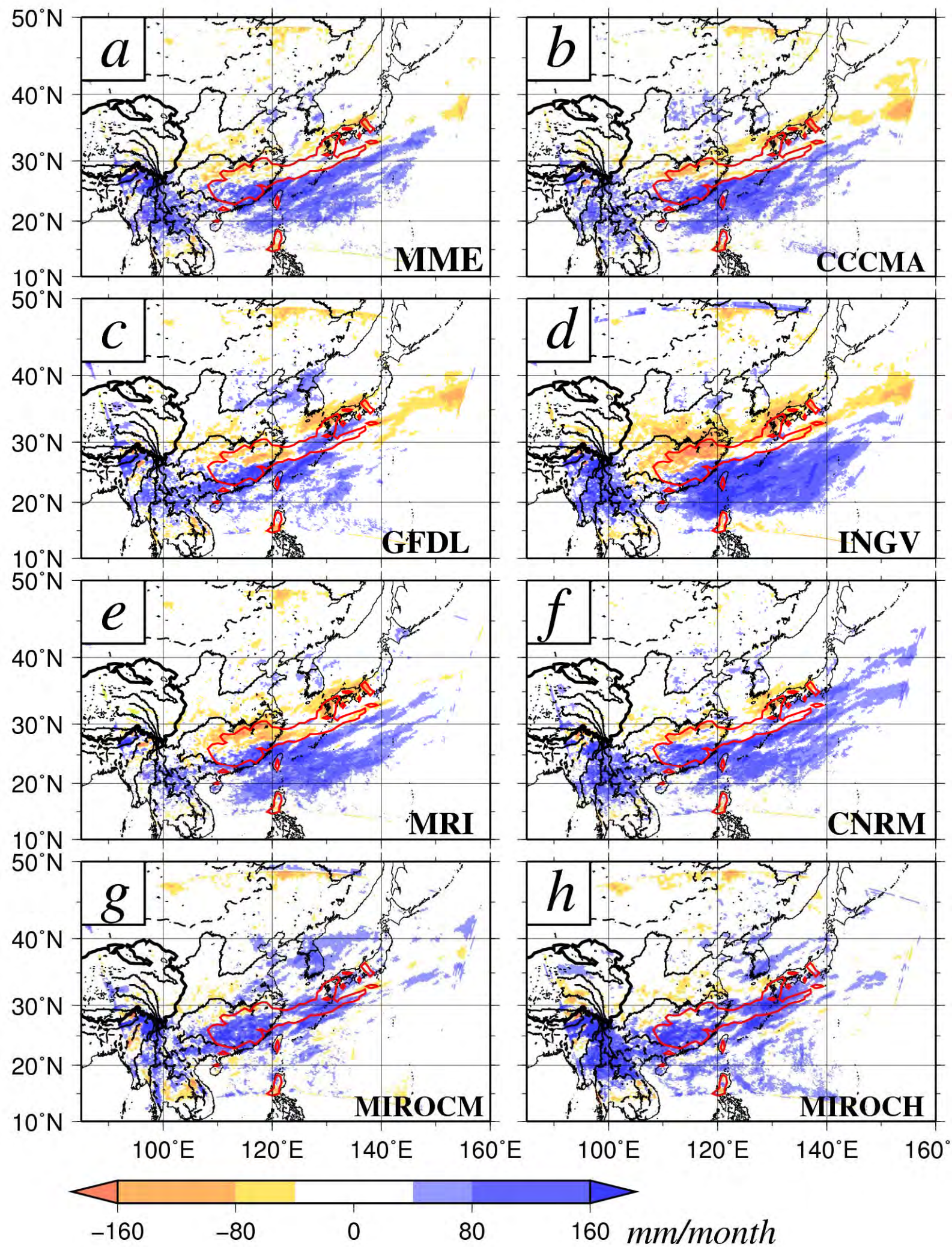


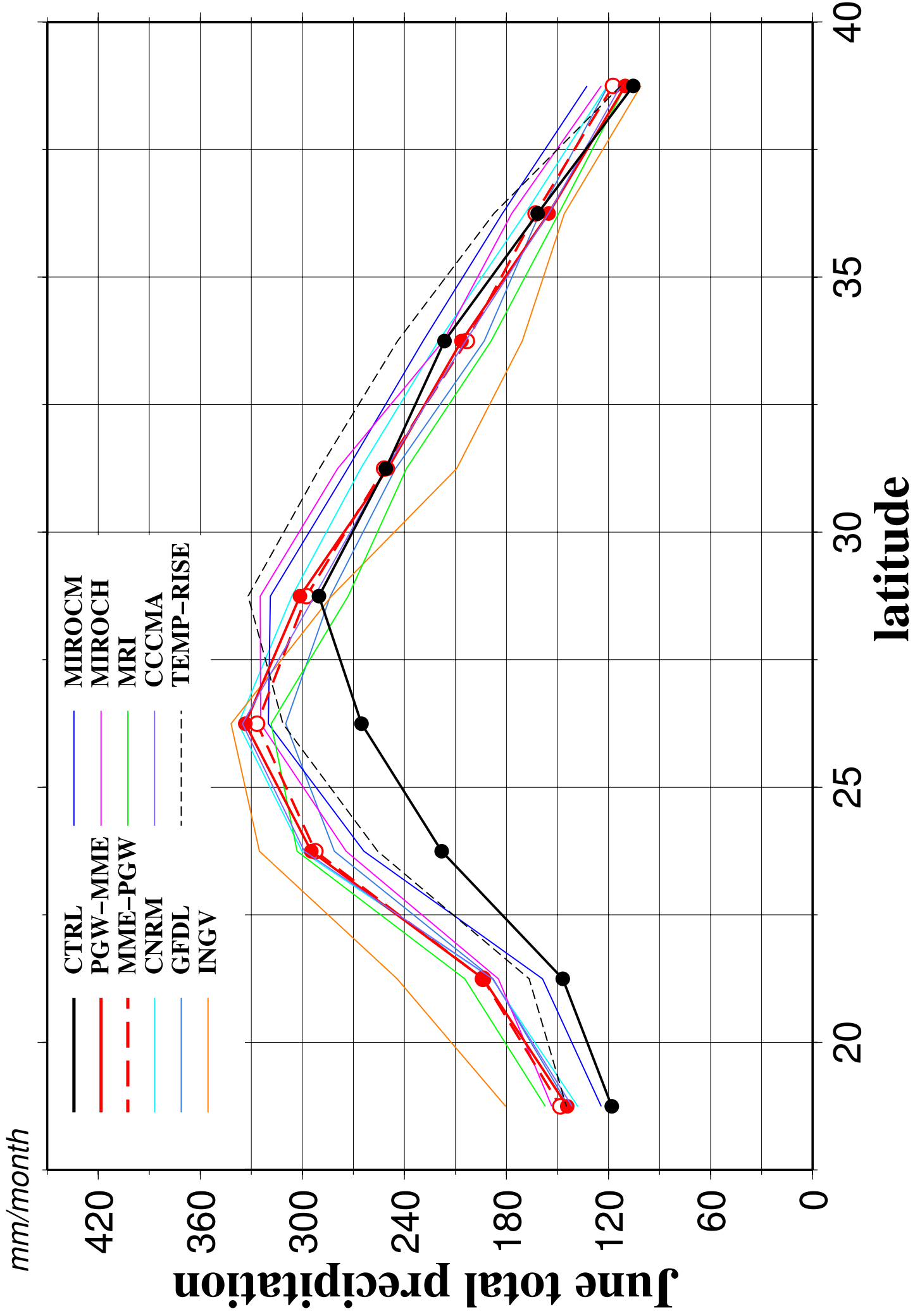


DDS: Dynamical Downscaling
RCM: Regional Climate Model



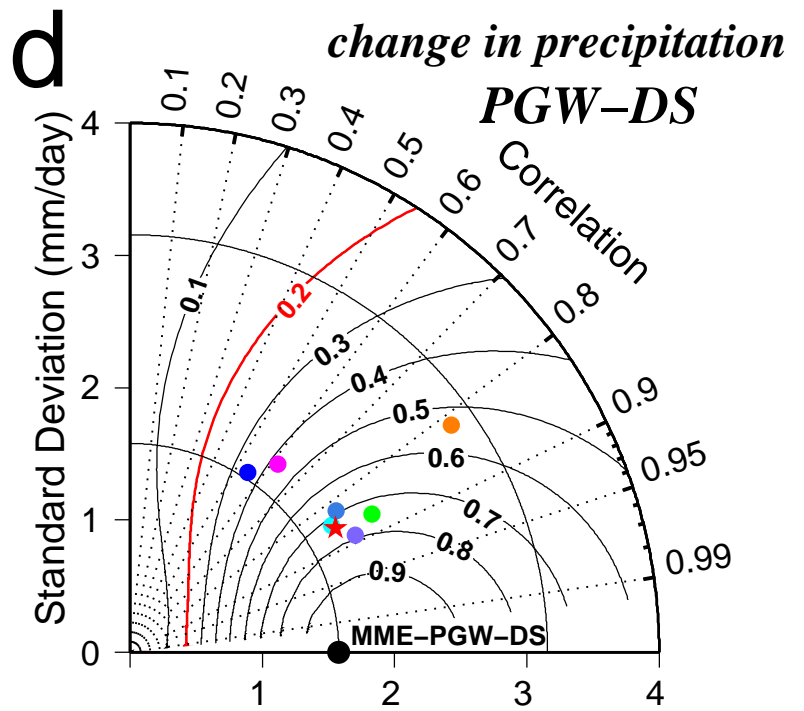
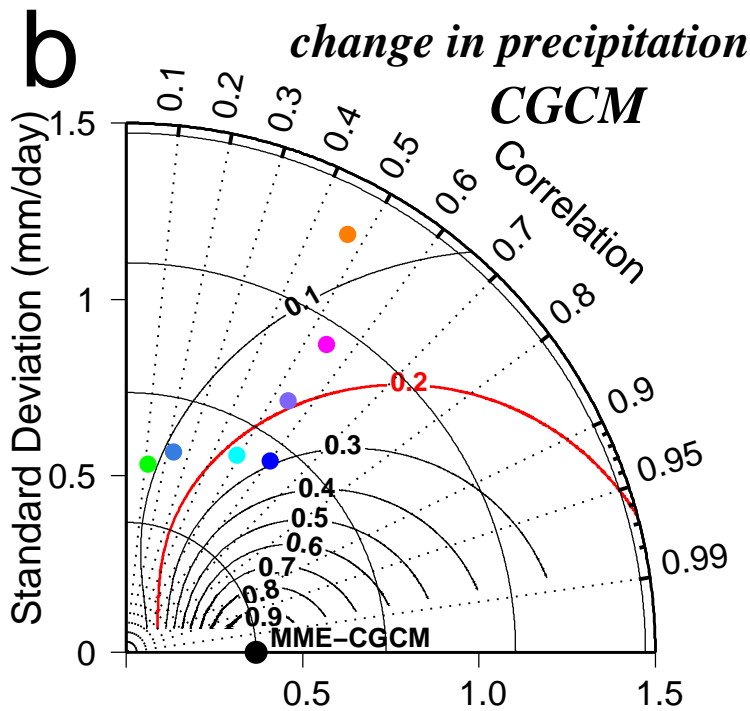
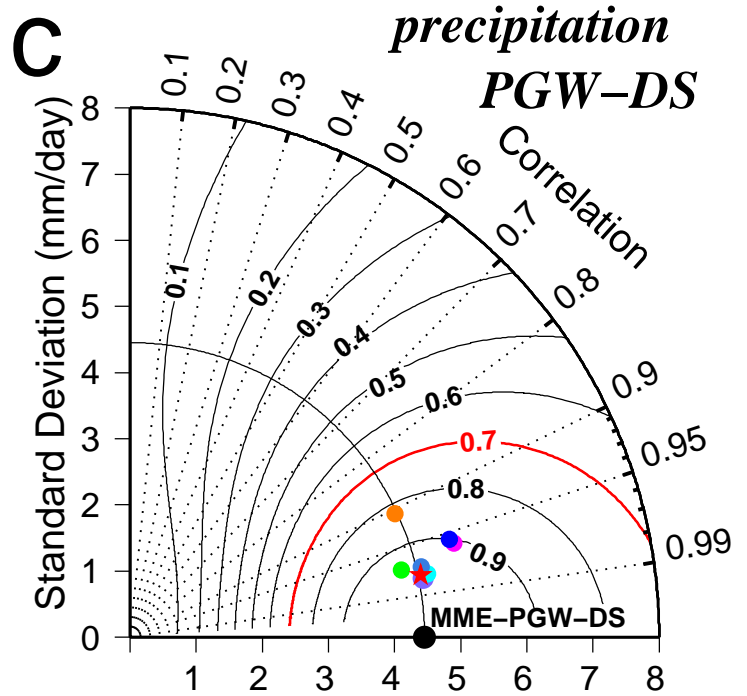
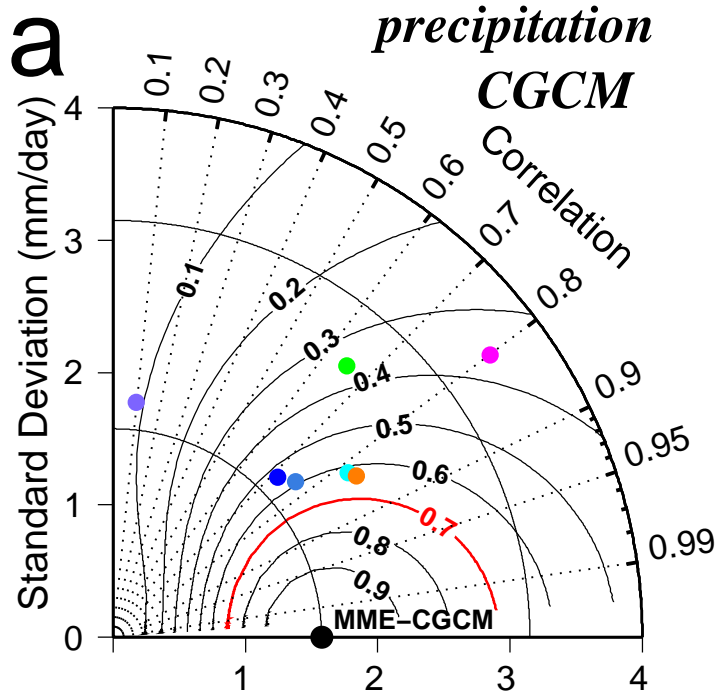


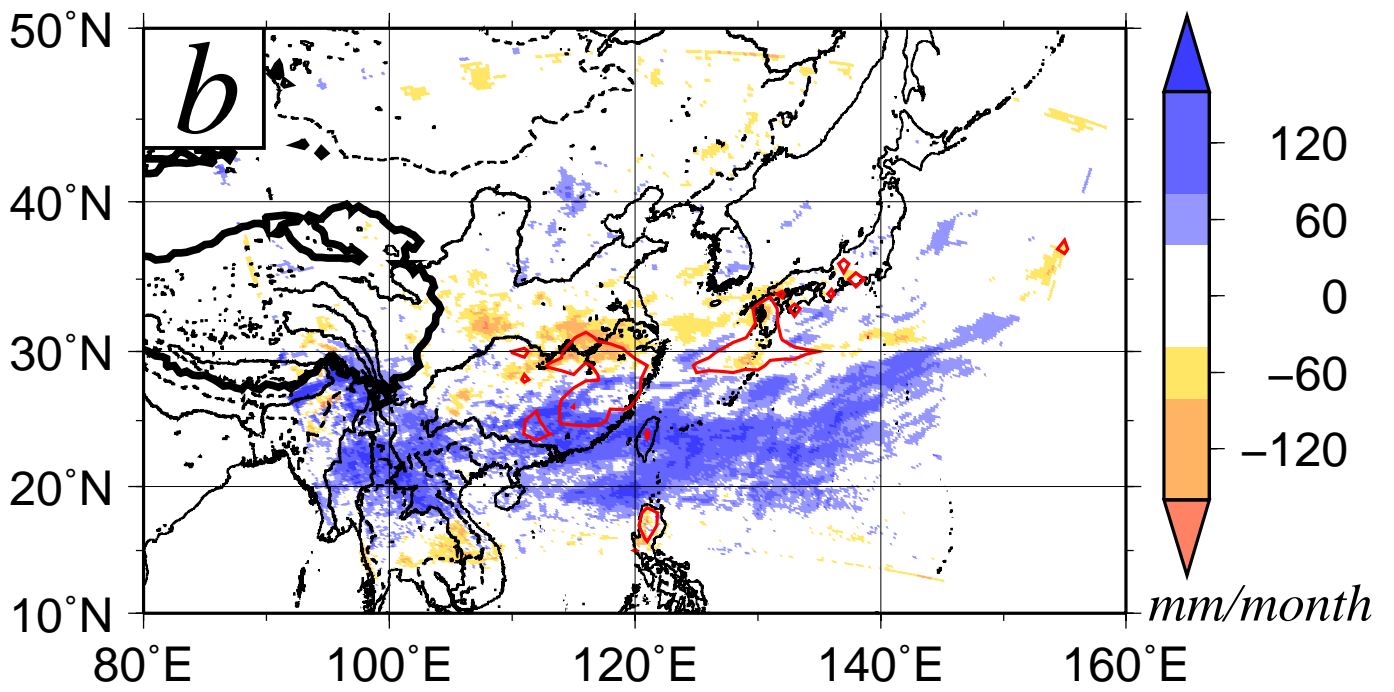
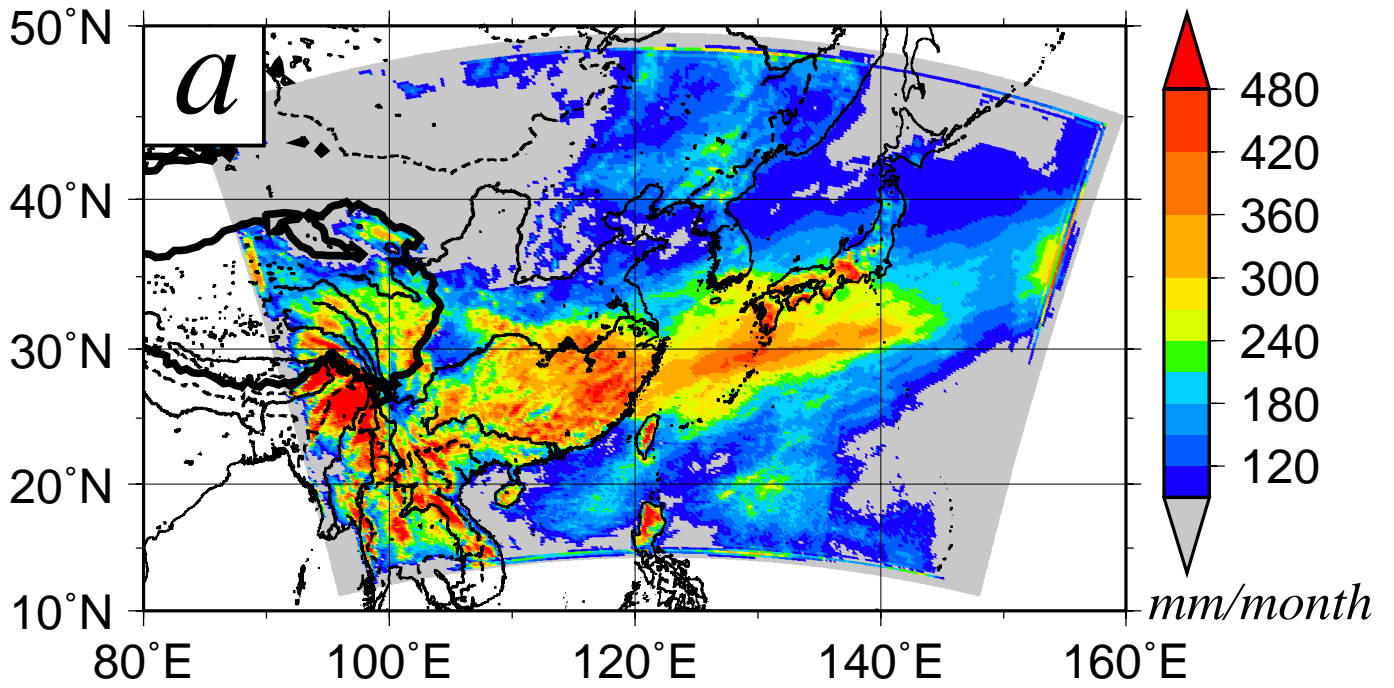


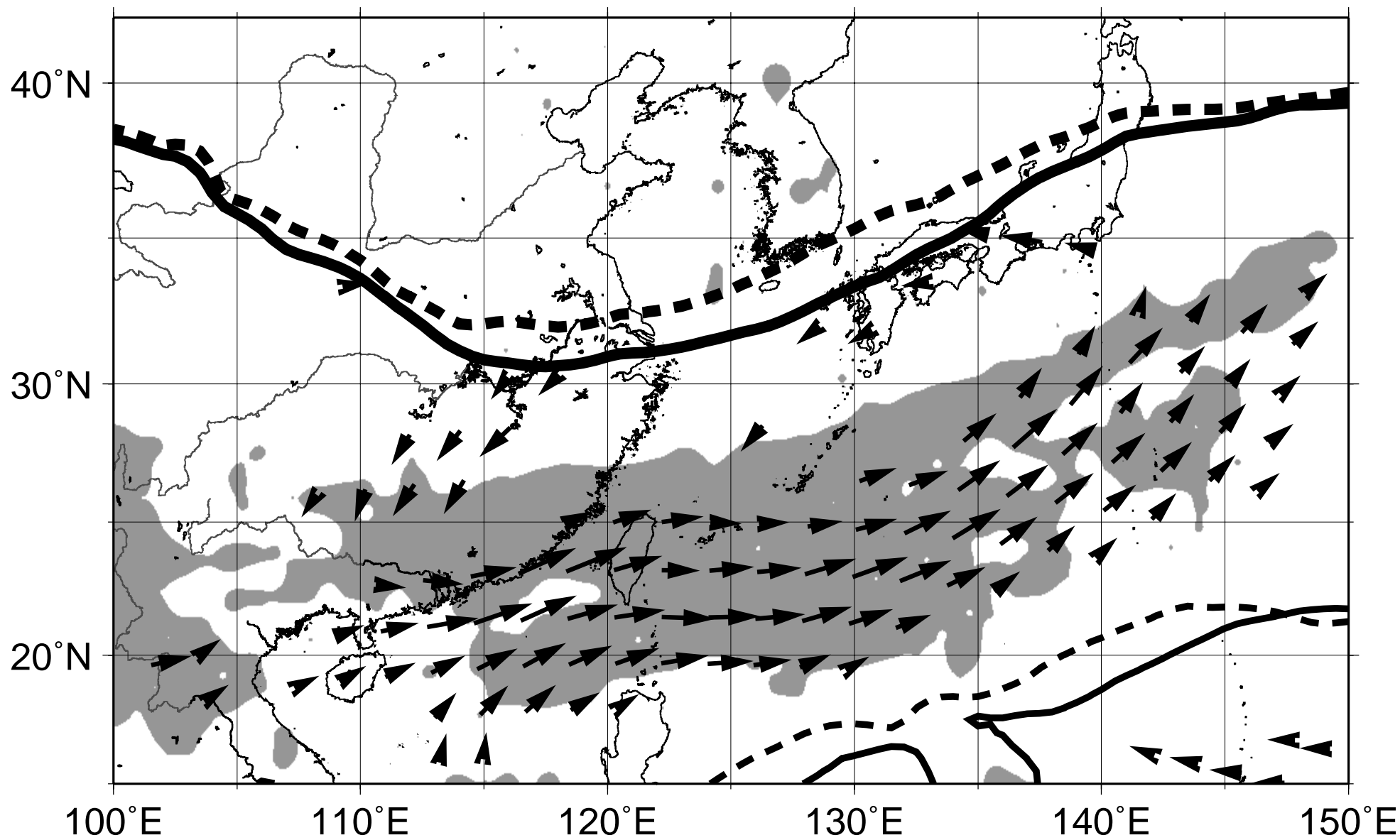


MME Taylor diagram

- CCCMA
- CNRM
- GFDL21
- INGV
- MIROCH
- MIROCM
- MRI
- ★ PGW-MME







(vectors: over 10 [g/kg*m/s])

→
20 g/kg*m/s